JCI The Journal of Clinical Investigation

Heterozygous mutations in the C-terminal domain of COPA underlie a complex autoinflammatory syndrome

Selket Delafontaine, … , Jérôme Delon, Isabelle Meyts

J Clin Invest. 2024. https://doi.org/10.1172/JCI163604.

Research In-Press Preview **Immunology**

Graphical abstract

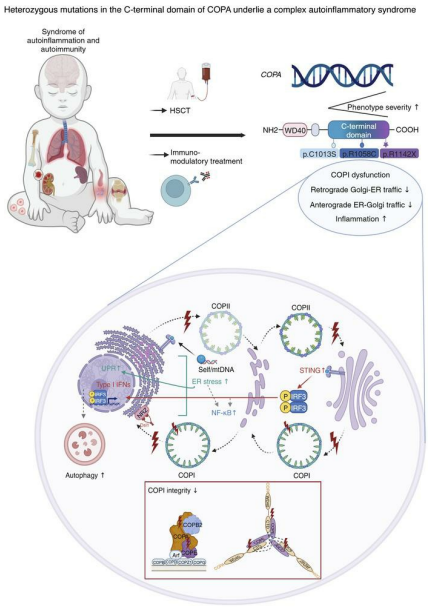

Find the latest version:

https://jci.me/163604/pdf

Heterozygous mutations in the C-terminal domain of COPA underlie a complex autoinflammatory syndrome

Selket Delafontaine[1,2,*], Alberto Iannuzzo[3,*], Tarin M. Bigley[4], Bram Mylemans[5], Ruchit Rana[6], Pieter Baatsen[7], Maria Cecilia Poli[8,9], Katrien Jansen[2], Daisy Rymen[2], Djalila Mekahli[10,11], Ingele Casteels[12], Catherine Cassiman[12], Philippe Demaerel[13], Alice Lepelley[14], Marie-Louise Frémond[14,15], Rik Schrijvers[16], Xavier Bossuyt[17], Katlijn Vints[7], Wim Huybrechts[18], Rachida Tacine[3], Karen Willekens[18], Anniek Corveleyn[18], Bram Boeckx[19,20], Marco Baggio[1], Lisa Ehlers[1], Sebastian Munck[21], Diether Lambrechts[19,20], Arnout Voet[5], Leen Moens[1], Giorgia Bucciol[1,2], Megan A. Cooper[4], Carla M. Davis[6], Jérôme Delon[3,**], Isabelle Meyts[1,2,**].

1. Laboratory for Inborn Errors of Immunity, Department of Microbiology, Immunology and Transplantation, KU Leuven, Leuven, Belgium, EU.
2. Department of Pediatrics, University Hospitals Leuven, Leuven, Belgium, EU.
3. Université Paris Cité, CNRS, INSERM, Institut Cochin, F-75014, Paris, France.
4. Department of Pediatrics, Division of Rheumatology/Immunology, Washington University in St. Louis, St. Louis, MO, 63110, United States.
5. Laboratory of Biomolecular Modelling and Design, Department of Chemistry, KU Leuven, Celestijnenlaan 200G, 3001 Leuven, Belgium.
6. Division of Immunology, Allergy and Retrovirology, Baylor College of Medicine, Texas Children's Hospital, 1102 Bates Avenue, MC 330.01, Houston, TX, 77030, USA.
7. Electron Microscopy Platform of VIB Bio Imaging Core, KU Leuven, Belgium.

8. Department of Pediatrics, Facultad de Medicina Clínica Alemana Universidad del Desarollo, Santiago, Chile
9. Immunology and Rheumatology unit, Hospital de niños Dr. Roberto del Rio, Santiago, Chile
10. PKD Research Group, Laboratory of Ion Channel Research, Department of Cellular and Molecular Medicine, KU Leuven, Leuven, Belgium.
11. Department of Pediatric Nephrology, University Hospitals Leuven, Leuven, Belgium.
12. University Hospitals Leuven, Department of Ophtalmology, Leuven, Belgium.
13. University Hospitals Leuven, Department of Radiology, Leuven, Belgium.
14. Université Paris Cité, Imagine Institute, Laboratory of Neurogenetics and Neuroinflammation, Inserm UMR 1163, Paris, France.
15. Paediatric Haematology-Immunology and Rheumatology Unit, Necker Hospital, AP-HP. Centre - Université Paris Cité, Paris, France.
16. KU Leuven, Allergy and Clinical Immunology Research Group, Department of Microbiology, Immunology and Transplantation, Leuven, Belgium.
17. KU Leuven, Clinical and Diagnostic Immunology, Department of Microbiology, Immunology and Transplantation, Leuven, Belgium.
18. Center for Human Genetics, Leuven University Hospitals, Leuven, Belgium.
19. Laboratory for Translational Genetics, Department of Human Genetics, KU Leuven, Leuven, Belgium.
20. VIB Center for Cancer Biology, Leuven, Belgium.
21. VIB Bio Imaging Core and VIB-KU Leuven Center for Brain & Disease Research, KU Leuven Department of Neurosciences, Leuven, Belgium.

* S. Delafontaine and A. Iannuzzo contributed equally to this paper. ** J. Delon and I. Meytscontributed equally to this paper. ✉ Correspondence to Isabelle Meyts: Herestraat 49, 3000 Leuven, Belgium; 0032 16 34 06 44; isabelle.meyts@uzleuven.be

Conflict of interest: IM has received consulting fee from Boehringer-Ingelheim (paid to KU Leuven) and from Takeda (paid to KU Leuven). IM has received a research grant from CSL-Behring (paid to KU Leuven). CM Davis receives research funding from the National Institutes of Health (NIH)/National Institute of Allergy and Infectious Disease (Consortium of Food Allergy Research (UM2 AI130836/ U01 AI126614) /Consortium of Eosinophilic Gastrointestinal Researchers), DBV Technologies, Aimmune Therapeutics, Regeneron Pharmaceuticals, Takeda and Allergenis.

Abstract

Mutations in the N-terminal WD40 domain of coatomer protein complex subunit α (*COPA*) cause a type I interferonopathy, typically characterized by alveolar hemorrhage, arthritis and nephritis. We described three heterozygous mutations in the C-terminal domain (CTD) of COPA (p.C1013S, p.R1058C and p.R1142X) in six children from three unrelated families with a similar syndrome of autoinflammation and autoimmunity. We showed that these CTD COPA mutations disrupt the integrity and the function of the coat protein complex I (COPI). In $COPA^{R1142X}$ and $COPA^{R1058C}$ fibroblasts we demonstrated that COPI dysfunction causes both an anterograde ER-to-Golgi and a retrograde Golgi-to-ER trafficking defect. The disturbed intracellular trafficking resulted in a cGAS/STING-dependent upregulation of the type I IFN signaling in patients and patient-derived cell lines, albeit through a distinct molecular mechanism in comparison to mutations in the WD40 domain of COPA. We showed that CTD COPA mutations induce an activation of the ER stress and NF-κB signaling in patient-derived primary cell lines. These results demonstrate the importance of the integrity of the CTD of COPA for COPI function and homeostatic intracellular trafficking, essential to ER homeostasis. CTD COPA mutations result in disease by increased ER stress, disturbed intracellular transport and increased pro-inflammatory signaling.

Introduction

The *COPA* gene encodes coatomer protein complex subunit α (COPA) (1). COPA was described in 1991 as a coat subunit of Golgi-derived non-clathrin coated vesicles, later termed 'coatomer' (2, 3). Coatomer or coat protein complex I (COPI) is ubiquitously expressed and localizes to the Golgi apparatus, cytosol and endoplasmic reticulum (ER) (4, 5). In mammalian cells, subunits α, β' and ε form the outer-coat subcomplex, while the adaptor subcomplex comprises the β, γ, δ and ζ subunit (6). Upon activation by brefeldin A-sensitive guanine nucleotide-exchange factor (GEF), coatomer is recruited to the target membrane, where it captures cargo molecules and polymerizes into spherical cages that mold the membrane into a COPI coated bud (7, 8). Ultimately, cargo-incorporated COPI vesicles are released in the cytosol (9). COPI and coat protein complex II (COPII) are essential for the intracellular vesicular transport of proteins in eukaryotic cells (10). While COPII transports newly synthesized proteins from the endoplasmic reticulum to the Golgi apparatus, COPI retrieves ER-resident cargo proteins from the Golgi apparatus or ER-Golgi intermediate compartment (ERGIC) to the ER to ensure their steady-state distribution (11, 12). Recently, COPI has been discovered to be required for early endosome maturation, autophagy and lysosomal trafficking (13, 14).

In 2015, heterozygous dominant negative mutations affecting a narrow stretch of 14 amino acids in the WD40 domain located in the N-terminal domain of COPA, were shown to underlie autosomal dominant COPA syndrome (Online Mendelian Inheritance in Man (OMIM) 616414) (15). Patients typically present with a triad of interstitial lung disease with or without pulmonary hemorrhage, inflammatory arthritis and immune complex-mediated nephropathy (16).This condition displays incomplete penetrance. Seventy-five patients with mutations in the N-terminal domain of COPA

have been described until now, with great variability both in terms of age of onset and clinical severity (15, 16, 25–33, 17–24). The mutations do not affect COPA protein expression, but they impair the retrograde Golgi-to-ER retrieval of dilysine-tagged ER-resident proteins, such as Surfeit locus protein 4 (*SURF4*) and indirectly Stimulator of Interferon Genes (*STING*) (17, 34-35). STING is a crucial immune sensor for multiple cytoplasmic nucleic acid sensors such as cyclic GMP-AMP synthase (*cGAS*) (36). Upon sensing of double-stranded DNA, cGAS synthesizes 2'-3'-cyclic GMP-AMP (2'3'-cGAMP), which binds STING and induces STING dimerization and its ER-to-Golgi translocation in COPII vesicles (37). Downstream signaling through TANK-binding-kinase 1 (TBK1)-mediated activation of transcription factors NF-κB and IFN regulatory factor 3 (IRF3) results in the expression of pro-inflammatory cytokines including type I and III interferon (IFN) (36). Failure of STING retrieval to the ER causes its constitutive activation at the Golgi and constitutive type I IFN signaling (17). In overexpression systems, this type I IFN signaling was demonstrated to have a variable cGAS dependency (17, 36). Furthermore, expression of mutant COPA results in ER stress, impaired autophagy and a skewing of CD4+ T cells towards a T helper type 17 (T_H17) phenotype (15).

The C-terminal domain (CTD) of COPA remains less well defined. It is essential for COPI integrity through the binding of the coatomer protein complex subunit ε, COPE, and the homo-oligomerization of COPA-COPE dimers (38). Additionally, the CTD plays a role in vesicle tethering to the endoplasmic reticulum (ER) (39, 40). In yeast cells, dysfunction and instability of COPI was induced by respectively a deletion of 170 residues and a point mutation in the CTD of *COPA* (38, 41). Here we investigate and functionally validate 3 heterozygous mutations in the C-terminal domain of COPA in 6 patients from 3 unrelated families.

Results

Autoinflammation and autoimmunity in six children from three unrelated families.

We identified six patients in three unrelated families (**Figure 1, Supplemental Table 1, Supplemental Figure 1, Full case report in Supplement, Supplemental Table 5).** The phenotype of these patients ranged from extremely severe (2/6) to mild (4/6). Patient 1 (A.II.3) presented at the age of 8 y.o. with anti-aquaporin-4 antibody-positive neuromyelitis optica **(Figure 1B)**. During the following years, she suffered from relapses of neuromyelitis optica and transverse myelitis **(Figure 1B)**. Despite extensive immunosuppressive regimens, she developed hepatosplenomegaly, cirrhosis, intra-abdominal lymphadenopathy, progressive pancytopenia and alveolar hemorrhage **(Figure 1B)**. At the age of 15 years 6 months, she received a hematopoietic stem cell transplantation. Patient 2 (B.II.1) presented at the age of 5 y.o. with livedo reticularis, acrocyanosis, heat hypersensitivity, somnolence, and an unusual sleep-wake cycle. He suffered from recurrent alveolar hemorrhage, unresponsive to extensive immunomodulatory treatment **(Figure 1C)**. He succumbed two years after his initial presentation due to secondary hemophagocytic lymphohistiocytosis (HLH) and multiple organ failure (MOF). Of note, none of the patients suffering from WD40 COPA mutations have deceased outside the context of lung transplantation. Patient 3 (C.II.1) presented at 5 y.o. with IgA nephropathy, which necessitated prolonged immunosuppressive treatment. His sister, patient 4 (C.II.2), was affected by a neuroblastoma at 12 y.o. During follow-up she developed arterial hypertension, stage II kidney disease, complex regional pain syndrome and vasculitis of the legs. Patient 5 (C.II.3) and 6 (C.II.4), prematurely born dizygotic twins, both suffered from recurrent upper respiratory tract infections. Patient 6 (C.II.4) developed a neonatal alveolar hemorrhage. All siblings of family C suffered from

recurrent arthralgia, which resolved with non-steroidal anti-inflammatory drugs. Autoantibodies were detected in 3 out of 6 patients (**Supplemental Table 2**). Patient 1 (A.II.3) showed a high percentage of HLA-DR positive T-cells and a low percentage of naive T- and B-cells, prior to treatment with Rituximab (**Supplemental Table 3)**. Furthermore, CD4+ T-cells of patient 1 (A.II.3) did not demonstrate a significant increase in the frequency of T_H17 cells **(Supplemental Figure 2A)**. Immunophenotyping of patient 2 (B.II.1) was unremarkable. Patient 3 (C.II.1) had a mildly elevated percentage of HLA-DR+ T-cells and patient 4 (C.II.2) a low percentage of B-cells. Naïve T-cell percentages were low for patients 3-5 (C.II.1-3). Immunophenotyping of patient 6 (C.II.4) was unavailable (**Supplemental Table 3)** (42).

Three heterozygous mutations in the C-terminal domain of COPA in patients.

Whole-exome sequencing (WES) was performed on all patients and their parents, except patient 6 (C.II.4) and B.I.1. Three heterozygous mutations, one nonsense and two missense, exclusively affecting the CTD of COPA, were detected (**Figure 2A**). Patient 1 (A.II.3) and her father (carrier 1, A.I.1) were heterozygous for the c.3424C>T (p.R1142X) variant. This variant was private and predicted to be deleterious through the generation of a premature stop codon. Patient 2 (B.II.1) and his mother (carrier 2, B.I.2) were heterozygous for the c.3172C>T (p.R1058C) variant. The four patients of family C (patients 3-6, C.II.1-4) and their father (carrier 3, C.I.1) were heterozygous for the c.3038G>C (p.C1013S) variant. The missense mutations, p.R1058C and p.C1013S, had a respective allele frequency of 0.000017 and 0.000010 in GnomAD and were predicted to be pathogenic by *in silico* prediction algorithms, which attributed a greater pathogenic potential to the p.R1058C mutation compared to the p.C1013S mutation **(Figure 2B; Supplemental Table 4)** (43–46). Sequence homology was highly conserved at the site of the

identified mutations in distantly related eukaryotes **(Figure 2C)**. All variants were confirmed by Sanger sequencing **(Figure 1A)**.

First, we analyzed the impact of these mutations on the expression of COPA, and its closest binding partners COPB2 and COPE, both on mRNA and protein level. Quantitative Reverse Transcription PCR (RT-qPCR), using 4 probes covering exon 2-3, exon 4-5, exon 11 and exon 32-33 of *COPA*, revealed a significantly reduced *COPA* level, in cDNA extracted from whole blood of patient 1 (A.II.3), for each *COPA* probe **(Figure 3A)**. Subsequently, the mean *COPA* level, expressed as the mean of the *COPA* levels determined using the 4 *COPA* probes, demonstrated a significantly reduced *COPA* mRNA level in patient 1 (A.II.3) and carrier 1 (A.I.1) **(Figure 3B)**. Based upon these results we suspected nonsense mediated decay of the $COPA^{R1442X}$ allele, although Sanger sequencing of *COPA* cDNA extracted from whole blood of patient 1 (A.II.3) and carrier 1 (A.I.1) detected wild-type (WT) and mutant *COPA* transcripts (**Supplemental Figure 2B**). Furthermore, *COPA* mRNA levels tended to be reduced in patient 2 (B.II.1), patients 3-6 (C.II.1-4) and carrier 3 (C.I.1), while carrier 2 (B.I.2) demonstrated levels in the range of controls **(Figure 3A)**. *COPB2* mRNA expression was significantly reduced in whole blood of patient 1 (A.II.3), patient 3 (C.II.1) and patient 5 (C.II.3), and tended to be reduced for the remaining patients and carriers **(Figure 3B)**. The *COPE* expression tended to be reduced for all patients and carrier 3 (C.I.1) **(Figure 3B).** In contrast, *COPA, COPB2* and *COPE* mRNA levels did not significantly differ from controls in patients' and carriers' EBV-transformed lymphoblastoid B-cells (EBV LCLs) and fibroblasts (**Supplemental Figure 3A-B)**.

Next, protein expression of COPA was analyzed in peripheral blood mononuclear cells (PBMCs) of patient 1 (A.II.3) and carrier 1 (A.I.1). COPA expression in $COPA^{R1142X}$ PBMCs, analyzed with an antibody specific for the N-terminal region of COPA, tended to be reduced, while

immunoblotting with an antibody targeted against the C-terminal amino acid 1150 of COPA revealed a significantly reduced COPA expression. Further, COPB2 protein level was reduced in PBMCs of patient 1 (A.II.3) and finally COPE expression tended to be reduced in both patient and carrier 1 (**Figure 3C-D**). A truncated COPA protein could not be detected (**Figure 3C**). COPA, COPB2 and COPE protein expression in COPA^{C1013S} PBMCs of carrier 3 (C.I.1) and patients 4-6 (C.II.2-4) was normal **(Supplemental Figure 3C)**. Consistent with the findings at mRNA level, COPA, COPB2 and COPE protein levels were similar in EBV LCLs, derived from patients and carriers of family A and C, and in fibroblasts, of patient 1 (A.II.3), carrier 1 (A.I.1) and patient 2 (B.II.1) compared to controls **(Figure 3E-F).**

COPA mutations impact COPI integrity by disrupting COPI formation (COPA^{R1142X}) or COPI stability (COPA^{R1058C} and COPA^{C1013S}).

To further evaluate the effect of the mutations on the integrity of COPI, we first generated 3D models of mutant COPA protein structures and evaluated their interaction with COPE **(Figure 2D)**. COPA^{R1142X} was predicted to encode a truncated protein, lacking 84 amino acids of itsC-terminal tail. The missing residues include on the one hand the dimerization interface between different COPA-COPE complexes and on the other hand the hydrophobic residues that pack together with α-helices, forming the binding site of COPE. COPA^{R1142X} was predicted to alter the conformation of the entire CTD and subsequently prevent COPA homo-oligomerization and COPE binding **(Figure 2D)**. R1058 and C1013 are located in the α-helices composing the main body of the CTD. COPA^{R1058C} and COPA^{C1013S} likely disrupt the conformation of the α-helices and change the protein's overall structure. Analysis of COPA^{R1058C} demonstrated that the mutation of the solvent exposed R1058 to a hydrophobic cysteine presumably affects the stability of COPA.

Further, this cysteine could form an unwanted disulfide bond with other free cysteines during protein folding, which is predicted to heavily disrupt the α-helix **(Figure 2D).** For $COPA^{C1013S}$, the mutation of C1013 to a serine was predicted to decrease the affinity towards the neighboring helix, thus affecting overall protein stability or folding kinetics **(Figure 2D).** Furthermore, the α-helices, who comprise residue 1013 and 1058, form a binding site for singleton tryptophan motif (STM), a sequence crucial for COPA homo-oligomerization and ER-tethering of COPI vesicles **(Figure 2E)** (39). Therefore, CTD *COPA* mutations were predicted to affect COPA conformation and to hamper homo-oligomerization, which is essential for COPI integrity.

Next, we evaluated the interaction of mutant COPA with COPB2 and COPE through a co-immunoprecipitation (co-IP) assay. For this purpose, HEK293T cells were transiently transfected with Flag-tagged wild-type (WT) or mutant COPA, COPB2 and COPE and co-immunoprecipitation was performed with a Flag antibody. The ability of mutant COPA to bind COPB2 and COPE was evaluated by immunoblotting of the whole cell extract, marked as input, and of the IP, for COPA, COPB2 and COPE **(Figure 4A)**. $COPA^{D243G}$ was used as the representative of the WD40 domain mutations. The co-immunoprecipitation assay revealed that while $COPA^{WT}$, $COPA^{D243G}$, $COPA^{C1013S}$ and $COPA^{R1058C}$ were able to pull down COPB2 and COPE, $COPA^{R1142X}$ did not precipitate COPE and displayed a significantly reduced interaction with COPB2, confirming the predicted disruption of COPI formation by $COPA^{R1142X}$ (**Figure 4A-B**). Furthermore, immunoblotting using an antibody that detects the Flag-tag, revealed a comparable expression of COPA in the input of HEK293T cells transfected with $COPA^{D243G}$, $COPA^{C1013S}$, $COPA^{R1058C}$ and $COPA^{WT}$. In contrast, HEK293T cells transfected with $COPA^{R1142X}$ produced a truncated protein, which displayed a reduced expression compared to the WT or missense mutation COPA proteins, suggesting $COPA^{R1142X}$ instability **(Figure 4A)**.

Impaired anterograde ER-to-Golgi and retrograde Golgi-to-ER COP-dependent protein trafficking in COPA^{R1142X} and COPA^{R1058C} fibroblasts.

To evaluate the effect of the CTD COPA mutations on COPI function, we examined COPI-mediated intracellular trafficking in COPA^{R1142X} and COPA^{R1058C} fibroblasts. COPA^{C1013S} fibroblasts were unavailable. First, we evaluated the anterograde ER-to-Golgi transport with a Procollagen I (PCI) assay, which relies on the temperature-sensitive protein folding of PCI (47). PCI exit from the ER occurs in COPII vesicles and depends on the retrograde recruitment of coat protein complex I (COPI)-coated ERGIC53-containing vesicles (48). The existence of this early COPI-dependent, pre-Golgi cargo sorting step was first demonstrated in mammalian cells and results in a delayed collagen secretion and retention of PCI in the ER in COPB2 siRNA-treated fibroblast (47, 49). COPA^{R1142X} fibroblasts derived from patient 1 (A.II.3) and carrier 1 (A.I.1), and COPA^{R1058C} derived from patient 2 (B.II.1), demonstrated a delayed ER export to the Golgi of PCI, which was retained at the ER, with higher levels of PCI in the ER for up to 60 minutes after the release of the 40°C temperature block, in line with a disturbed COPI function **(Figure 4C-D)**. Accumulation of PCI in both COPA^{R1142X} and COPA^{R1058C} fibroblasts was also demonstrated by an increased intensity of PCI 60 minutes after the release of the 40°C temperature block, whereas control cells showed a 50% reduction in their amount of PCI **(Supplemental Figure 4)**. The retention of PCI in mutant cells is most likely due to a defect in secretion.

Secondly, we performed an assay to measure the retrograde transport of Cholera toxin B subunit (CtxB) (50). COPA^{R1142X} fibroblasts derived from patient 1 (A.II.3) and carrier 1 (A.I.1), and COPA^{R1058C} fibroblasts derived from patient 2 (B.II.1), demonstrated a delayed Golgi-to-ER trafficking, with higher levels of CtxB at the Golgi for up to 10 hours after exposure to CtxB **(Figure 4E-F)**. Next, we evaluated COPA^{R1142X} fibroblasts of patient 1 (A.II.3) by electron

microscopy to examine both the morphology of the COPI vesicles, as well as the impact of COPI dysfunction on cellular morphology. As previously described for COPB2 deficient fibroblasts, we found an increased accumulation of coated vesicles in the cytosol and the Golgi apparatus appeared smaller in COPA^{R1142X} fibroblasts in comparison to healthy control fibroblasts **(Figure 4G)** (47)**.** In conclusion, the impaired ER exit of PCI, the retention of CtxB at the Golgi in COPA^{R1142X} and COPA^{R1058C} fibroblasts, and the disturbed cellular morphology in COPA^{R1142X} fibroblasts demonstrate a disruption of both the anterograde COPII-dependent ER-to-Golgi transport and retrograde COPI-dependent Golgi-to-ER transport caused by COPI dysfunction.

Type I IFN signaling is increased in 3 out of 6 patients with CTD COPA mutations and does not correlate with disease severity.

Next, we examined whether mutations in the CTD of COPA, analogous to the mutations in the WD40 domain, induce type I interferon signaling. Therefore, we assessed 6 interferon-stimulated genes (ISGs) by RT-qPCR in RNA extracted from whole blood or PBMCs. In patients 1 (A.II.3), 2 (B.II.1) and 6 (C.II.4) we measured an elevated type I IFN score **(Figure 5A)** (51). Patient 1 (A.II.3) and 2 (B.II.1), affected by a more severe phenotype, displayed at least on one occasion an elevated type I IFN score within the range seen in STING-associated vasculopathy with onset in infancy (SAVI) or Aicardi-Goutières syndrome (AGS) patients, while patient's 6 (C.II.4) score was markedly lower. Although all siblings of family C are symptomatic, only patient 6 (C.II.4) demonstrated an elevated type I IFN score. Asymptomatic carriers and healthy family members demonstrated no or a minimally elevated type I IFN score. Despite disease progression, serial follow-up of IFN scores of patient 1 (A.II.3), derived from thirteen different time points over a period of one and a half years, decreased, in line with the C-reactive protein (CRP) values

(Figure 5B) (17)**.** This contrasts with the persistently elevated type I IFN score described in patients affected by WD40 domain COPA mutations (17). IFN signaling through Signal Transducer and Activatorof Transcription 1 (*STAT1*) was shown by flow cytometric evaluation of downstream phosphorylated STAT1 (pSTAT1) in monocytes of patient 1 (A.II.3). Upon blocking of phosphatases and IFN-γ stimulation, there was a significantly higher phosphorylation of STAT1 in patient 1 (A.II.3) compared to both a healthy control and a STAT1 gain-of-function (GOF) patient, heterozygous for the c.A1159G (p.T387A) mutation in *STAT1* (**Figure 5C**). Further, co-localization demonstrated increased levels of STING in the Golgi of $COPA^{R1142X}$ and $COPA^{R1058C}$ fibroblasts, and $COPA^{R1142X}$ and $COPA^{C1013S}$ EBV LCLs compared to controls **(Figure 5D-E)**. Finally, the ratio of SIGLEC-1 positive monocytes, as a surrogate marker of type I IFN signaling environment, was significantly higher for patient 1 (A.II.3) in comparison to controls **(Supplemental Figure 5A).** In conclusion, these data demonstrate an upregulation of type I IFN signaling due to CTD COPA mutations in several patients, patient-derived fibroblasts and EBV LCLs.

Overexpression of the CTD COPA mutants does not induce STING-dependent type I IFN signaling in HEK293T cells.

To further study the type I IFN signaling in CTD COPA mutations, HEK293T cells, which endogenously express COPA and lack STING and cGAS, were transiently transfected with STING and WT or mutant COPA. $COPA^{D243G}$ served as the representative of WD40 domain COPA mutations. Western blot analysis of phosphorylated IRF3 (p-IRF3) tended to be reduced in HEK293T cells co-transfected with STING and $COPA^{R1058C}$ or $COPA^{R1142X}$, while HEK293T cells co-transfected with STING and $COPA^{C1013S}$ expressed similar p-IRF3 levels compared to

HEK293T cells overexpressing STING and $COPA^{WT}$ (**Figure 6A-B**). In contrast, $COPA^{D243G}$ induced significantly increased p-IRF3 levels (**Figure 6A-B**). Consistently, *IFIT1* mRNA expression was enhanced in HEK293T cells co-transfected with $COPA^{D243G}$ and STING, while HEK293T cells co-transfected with STING and CTD COPA mutants demonstrated a similar, for $COPA^{C1013S}$, or reduced, for $COPA^{R1058C}$ and $COPA^{R1142X}$, level of *IFIT1* in comparison to cells overexpressing WT COPA and STING (**Figure 6C**). Similar differences, yet statistically insignificant, were noted upon evaluation of *ISG15* mRNA expression (**Figure 6C**). An Interferon Stimulated Response Element (ISRE) luciferase assay confirmed a comparable, for $COPA^{C1013S}$, or reduced, for $COPA^{R1058C}$ and $COPA^{R1142X}$, ISRE activation in HEK293T cells co-transfected with CTD mutant COPA and STING in comparison to HEK293T cells overexpressing STING and WT COPA (**Figure 6D).** Finally, confocal microscopy proved a similar co-localization of STING with Golgi matrix protein 130 (GM130), a peripheral membrane protein of the cis-Golgi, in HEK293T cells co-transfected with CTD mutant COPA and STING in comparison to cells overexpressing WT COPA and STING, while an increased co-localization was noticed in HEK293T cells co-transfected with $COPA^{D243G}$ and STING (**Figure 6E-F).** To decipher whether the perturbation of STING-dependent type I IFN signaling, caused by CTD COPA mutations, was a dominant negative or haploinsufficient effect, we evaluated *IFIT1* mRNA expression in HEK293T cells co-transfected with on the one hand varying ratios of WT COPA, mutant COPA and empty vector (EV) of COPA and on the other hand EV of STING or WT STING **(Figure 6G, Supplemental Figure 5B).** The variants which reduce the *IFIT1* expression below the level corresponding to 50% WT COPA are considered to be dominant negative. We observed a dominant negative (DN) effect of CTD mutant COPA on *IFIT1* induction, since the *IFIT1* expression in HEK293T cells transfected with CTD COPA mutant, WT COPA and STING was

consistently reduced in comparison to the *IFIT1* levels in HEK293T cells overexpressing identical amounts of EV of COPA, WT COPA and STING **(Figure 6G).**

In conclusion, overexpression of the CTD COPA mutations in HEK293T cells did not induce increased type I IFN signaling, in contrast with the strong upregulation of type I IFN signaling by $COPA^{D243G}$, pointing to a different mechanism.

CTD COPA mutations cause activation of ER stress and pro-inflammatory signaling pathways such as the NF-κB pathway.

Next we investigated whether dysregulation of other inflammatory signaling pathways could contribute to the clinical phenotype and type I IFN signaling observed in patients. We hypothesized that the defective intracellular trafficking caused by CTD COPA mutations increases ER stress and activates the unfolded protein response (UPR), similarly to the effects of mutations in the WD40 domain of COPA (15). Indeed, in $COPA^{R1142X}$, derived from patient 1 (A.II.3) and carrier 1 (A.I.1), and $COPA^{R1058C}$ fibroblasts, derived from patient 2 (B.II.1) we found an increased expression of the molecular chaperone binding immunoglobulin protein (BiP) by confocal microscopy, both in baseline conditions as well as after stimulation with thapsigargin **(Figure 7B)**. BiP is suggested to act as a primary sensor in the activation of the UPR, which is a stress response activated to restore cellular homeostasis. After treatment with thapsigargin, whichinduces ER stress by inhibiting the sarco-/endoplasmic reticulum Ca2+-ATPase (SERCA), qPCR evaluation of 3 UPR-dependent genes (*HSPA5*, *ATF4* and *DDIT3*) showed a significantly elevated level of *HSPA5* and *ATF4* in thapsigargin-treated EBV LCLs of patient 1 (A.II.3) in comparison to controls **(Figure 7A)**. In contrast, $COPA^{R1142X}$ EBV LCLs derived from carrier 1 (A.I.1) did not reveal a statistically significant difference in comparison to controls. $COPA^{C1013S}$ EBV LCLs, derived from

patients 3 till 6 (C.II.3-6) and carrier 3 (C.I.1), demonstrated a tendency towards an increased UPR response upon ER stress induction **(Figure 7A)**. Furthermore, *DDIT3* mRNA expression was significantly elevated, for p.C1013S and p.R1142X, or tended to be elevated, for p.R1058C, in unstimulated HEK293T cells overexpressing the CTD COPA mutants in comparison to cells transfected with WT COPA **(Supplemental Figure 8).**

Secondly, we evaluated the translocation of the transcription factor family nuclear factor kB (NF-κB) which could potentially be induced by ER stress and could contribute to type I IFN signaling induction. Confocal microscopy in $COPA^{R1142X}$ and $COPA^{R1058}$ fibroblasts of patients (A.II.3 , B.II.1) and carrier (A.I.1), was performed to measure the intensity of p65 RelA in the nucleus and cytoplasm **(Figure 7C).** In unstimulated control fibroblasts, p65 is found almost exclusively in the cytosol while unstimulated $COPA^{R1142X}$ and $COPA^{R1058}$ fibroblasts demonstrate an increased nuclear presence of p65 indicating a constitutive activation of the NF-κB pathway caused by these CTD COPA mutations. In addition, $COPA^{R1142X}$ and $COPA^{R1058C}$ fibroblasts showed pronounced translocation after 1 hour of stimulation with LPS compared to controls. These findings were confirmed by immunoblotting of nuclear cell extract of TNF-α -stimulated fibroblasts for p65. Fibroblasts of patient 1 (A.II.3) and carrier 1 (A.I.1) showed an incresed and prolonged nuclear presence of p65 in comparison to controls **(Supplemental figure 6A-B).**

Finally, we evaluated the mRNA expression of inflammatory cytokines in EBV LCLs, at steady state and upon ER stress induction, by qPCR. $COPA^{R1142X}$ EBV LCLs of patient 1 (A.II.3) had increased transcript levels encoding interleukin *(IL)-1β*, both in the unstimulated and stimulated condition (**Supplemental Figure 7**). The transcript levels in EBV LCLs derived from carrier 1 (A.I.1), patients 3-6 (C.II.3-6) and carrier 3 (C.I.1) were not statistically significantly upregulated in both conditions. Further, evaluation of the serum cytokine concentrations of patient

1 (A.II.3), patient 2 (B.II.1) and 3 (C.II.1), demonstrated an increased Interferon γ (IFN-γ) concentration for patient A.II.3, and increased IL-6, IL-8 and TNF-α concentrations were detected for all patients. (**Supplemental Figure 5C**). These findings point to a complex interplay of various pro-inflammatory signaling pathways.

Transcriptome analysis by RNA sequencing of peripheral blood reveals an upregulation of the UPR and dysregulation of autophagy in CTD COPA patients.

RNA was extracted from whole blood of four healthy controls, two CTD COPA mutation carriers (carrier 1 and 3, respectively A.I.1 and C.I.1), five COPA patients (patient 1 and 3-6, respectively A.II.3 and C.II.1-4) and one SAVI patient, heterozygous for the c.463G>A (p.V155M) variant in *STING*, as a control. Principal component analysis of the p-values of significantly enriched genes in the transcriptome demonstrated clustering of the carriers, controls, SAVI patient and patient 3-6 (C.II.1-3), while patient 1 (A.II.3) and patient 6 (C.II.4) showed a distinct transcriptome profile **(Figure 7E)**. Therefore, patient 1 (A.II.3) and 6 (C.II.4) were compared to the group of carriers, controls, SAVI patient and patient 3-6 (C.II.1-3) by IPA analysis of the differential gene expression (**Figure 7F**). In patient 1 (A.II.3) autophagy was the pathway with the highest significance and likely activated, while in patient 6 (C.II.4) the autophagy pathway was mildly activated. Importantly, the analyzed RNA sample of patient 1 (A.II.3) was obtained 4 months after discontinuation of the treatment with Sirolimus, an autophagy inducer. Several genes involved in autophagy showed a strong activation in patient 1 (A.II.3) and a tendency for inhibition in patient 6 (C.II.4) **(Figure 7G).** In patient 6 (C.II.4), the Eukaryotic Initiation Factor 2 (eIF2) signaling pathway showed the highest statistical significance and appeared activated **(Figure 7F)**. Moreover, in patient 1 (A.II.3) the nuclear factor erythroid 2–related factor 2 (NRF2)-mediated central

cytoprotective pathway against oxidative stress, was activated **(Figure 7F).** Patient 1 (A.II.3) and patient 6 (C.II.4) both displayed an activation of the eIF2 signaling pathway **(Figure 7G)**. NRF2 and eIF2 are downstream targets of pancreatic ER kinase (PKR)-like ER kinase (PERK) and are two parallel pathways through which the unfolded protein response helps to increase survival in ER stressed cells (52). While the SAVI patient demonstrated a strong upregulation of several ISGs, patient 6 (C.II.4) showed a milder upregulation and a clear upregulation was absent for patient 1 (A.II.3), similar to the corresponding type I IFN score at day -86, as shown in Figure 5B (**Figure 7G)** (53). In conclusion, transcriptomic analysis revealed signatures of elevated ER stress and activated UPR as well as cytoprotective NRF2 regulated genes and activated autophagy.

Discussion

Here, we report 3 previously undescribed heterozygous mutations, 1 private nonsense and 2 missense, in the CTD of *COPA* in six children affected by a syndrome of autoinflammation and autoimmunity **(Supplemental Table 5).** Two reports mentioned mutations in the C-terminal domain of COPA, without functional validation (54, 55). Despite the many similarities with COPA syndrome caused by WD40 domain mutations, including the incomplete penetrance, the severe phenotype unresponsive to multiple lines of treatment in two out of six patients with CTD mutations, is striking. In terms of pathogenesis, we show that $COPA^{R1142X}$ impairs the interaction of COPA with COPB2 and COPE, considering the reduced expression of the truncated $COPA^{R1142X}$ upon overexpression in HEK293T cells. Binding of COPB2 and COPE remained intact for $COPA^{C1013S}$ and $COPA^{R1058C}$ in overexpression, although biomodelling suggested an impaired stability of COPI and a compromised tethering to the NRZ complex as a result of these mutations (40, 56-57). In line with these findings, the impaired anterograde ER export of PCI and

the impaired retrograde transport of CtxB evidence the resulting COPI dysfunction, at least in $COPA^{R1142X}$ and $COPA^{R1058C}$ fibroblasts (47, 50). Therefore, our data highlight the importance of the integrity of the CTD of COPA for COPI function and demonstrate the impact of CTD COPA mutations on COPI function and bidirectional COP-dependent transport of proteins between ER and Golgi (37).

We found an elevated type I IFN score in the peripheral blood of three patients and an Golgi accumulation and activation of STING in $COPA^{R1142X}$ and $COPA^{R1058C}$ fibroblasts and $COPA^{R1142X}$ and $COPA^{C1013S}$ EBV LCLs **(Figure 5).** However, serial evaluation of the type I IFN score of patient 1 (A.II.3) during the disease course demonstrated a poor correlation with disease severity, as previously observed in adenosine deaminase 2 deficiency (58). Furthermore, only one of the patients of family C, patient C.II.4, displayed an elevated IFN score. To gain further insight into the mechanism of type I IFN upregulation, we performed overexpression of the mutants in HEK293T cells. In contrast to mutations in the WD40 domain of COPA, CTD COPA mutations did not induce a STING-dependent type I IFN signaling upon overexpression in HEK293T cells, indicating a distinct mechanism of type I IFN activation (17). We further noticed a differential effect of the CTD COPA mutations on STING-dependent type I IFN signaling **(Figure 6),** which has previously been observed for WD40 domain COPA mutants, and which seems to reflect the severity of the clinical phenotype (17).

We hypothesize that the dominant negative effect of COPA CTD mutations on ISG expression, demonstrated in the overexpression model, is the result of an impaired intracellular protein transport. In line with this hypothesis, TBK1 phosphorylation and ISG expression are increased in mouse embryonic fibroblasts, mutated in the *COPA* WD40 domain. However,

treatment of these fibroblasts with Brefeldin A, an inhibitor of COPI vesicle formation and Golgi-to-ER transport (59), blocks these effects, suggesting that a complete inhibition of the COPI-dependent transport disrupts STING accumulation and activation at the Golgi. Previously, Steiner et al. have demonstrated that the deletion of different COPI subunit proteins, in particular COPA, COPG1 and COPD, induces cGAS-dependent STING activation (36). The authors prove that a defect in retrograde Golgi-to-ER trafficking causes mislocalization of STING to the Golgi. The activation of the type I IFN signaling however, was dependent on cGAS activation, which was considered to be a consequence of the altered cellular homeostasis in cells affected by COPI dysfunction. Our data demonstrate that the upregulated type I IFN signaling caused by CTD COPA mutants is secondary to an intracellular trafficking defect and we suggest that induction of type I IFN signaling occurs in a cGAS-dependent manner. cGAS is absent in HEK293T cells, but type I IFN pathway activation in vivo in patients can be driven through cGAS activation as an indirect result of the impaired intracellular trafficking and disturbed cellular homeostasis (36). As suggested by Steiner et al., disrupted cellular homeostasis could cause a secondary activation of cGAS by leakage of mitochondrial DNA into the cytoplasm, ER stress-induced Zinc release in the cytoplasm or accumulation of genomic self DNA in the cytoplasm (36).

Autoinflammation in CTD COPA likely results from the activation of multiple pro-inflammatory signaling pathways, next to the type I IFN pathway. First ER stress plays a complex role in the induction of inflammation (60). The impairment of the retrograde Golgi-to-ER transport caused by mutations in different COPI subunit proteins, was previously described to result in an increased ER stress in activated T- and/or B-cells, heterozygous for mutations in the WD40 domain of *COPA* or homozygous for mutations in *COPG1*, or unstimulated patient-derived

fibroblasts, heterozygous for mutations in *COPD* or homozygous for mutations in *COPB2* (47, 61-63). Similarly, we observed an increased ER stress in $COPA^{R1142X}$ and $COPA^{R1058C}$ fibroblasts and an upregulated UPR in activated EBV LCLs of $COPA^{R1142X}$ of patient 1. In $COPA^{C1013S}$ EBV LCLs this effect was less pronounced, although we observed a tendency towards an activation of the UPR**.** These data were supported by transcriptome analysis by RNA sequencing of peripheral blood of patient 1 (A.II.3) and 6 (C.II.4). A different pattern of UPR gene activation was noted in both patients. which could reflect a continuum between adaptive, in patient 6 (C.II.4), and maladaptive UPR response,in patient 1 (A.II.3) as well as the effects of different treatments (64).

We hypothesize that the increased ER stress and activation of the UPR could result from an impaired retrieval of chaperone proteins to the ER, due to a limited retrograde Golgi-to-ER retrograde transport, and the accumulation of nascent proteins in the ER, caused by an impaired ER-to-Golgi anterograde transport. This hypothesis is supported by the upregulation of *DDIT3* observed in HEK293Tcells overexpressing the CTD COPA mutants. Increased ER stress and UPR upregulation are therefore key pathogenic mechanisms caused by CTD COPA mutants. Although diverse inborn errors of immunity (IEI) underlie increased ER stress and UPR upregulation, the pathways leading to increased ER stress differ and this may at least in part contribute to the differential phenotypical expression.

Secondly, $COPA^{R1142X}$ and $COPA^{R1058C}$ fibroblasts demonstrate an activation of the NF-κB pathway and EBV LCLs of patient 1 (A.II.3) showed increased expression of *IL-1β*. Additionally the concentration of NF-κB related cytokines, such as IL-6 and TNF-α, were increased in the serum of patient 1, 2 and 3 (A.II.3, B.II.1, C.II.1). In contrast, the concentration of IL-6, IL-10 and TNF-α, was reportedly normal in the plasma of patients affected by mutations in the WD40 domain of COPA (17). Finally, transcriptome analysis of peripheral blood has revealed a dysregulation of

autophagy in patient 1 (A.II.3) and 6 (C.II.4), as previously demonstrated *in vitro* for mutations in the WD40 domain of COPA (15). COPI is indeed known to be obligatory for autophagy (65).

There are some limitations to this study. Although the CTD COPA mutations studied here, display a common disease-causing mechanism, the clinical and the cellular phenotype are heterogeneous, like for WD40 domain COPA mutations. As for the discrepancy between the ubiquitous expression of COPA versus the mostly immunological phenotype, we can only hypothesize that the strong expression of COPA in monocytes plays a role and that our understanding of the phenotype will continue to evolve with the description of additional patients.

In summary, mutations in the CTD of COPA, a previously unstudied domain, cause autoinflammation through a mechanism distinct from the N-terminal domain COPA mutations. The molecular mechanism however shows striking similarities with previously described coatopathies. We demonstrate that mutations in the CTD of COPA impair COPI integrity, which causes a disruption of COPII-dependent anterograde ER-to-Golgi and COPI-dependent retrograde Golgi-to-ER transport, at least in $COPA^{R1142X}$ and $COPA^{R1058C}$ fibroblasts. In our patients, we provide evidence for a concerted activation of several pro-inflammatory pathways including the ER stress and UPR and NF-kB signaling next to type I IFN signaling. Our report therefore expands the phenotype and genotype of COPA syndrome and highlights the crucial importance of the integrity of COPI and the COPI-dependent transport between Golgi and ER in the intracellular homeostasis. Our findings pave the way for the discovery of mutations in molecules who affect the COPI-dependent transport between Golgi and ER and underlie yet undetermined IEI.

Methods

Patients and sample collection.

Patients were recruited from the Inborn Errors of Immunity Department, University Hospitals Leuven (Leuven, Belgium), Pediatric Immunology and Rheumatology Department St. Louis Children's Hospital (Washington, USA), Pediatric Immunology, Allergy and Retrovirology Department Texas Children's Hospital (Houston, USA). Clinical and laboratory data were collected for all included patients. If possible**,** parents and siblings of the index case were also included. Blood samples were collected from individual members of family A (A.I.1, A.I.2, A.II.1-4), family B (B.I.2 and B.II.1) and family C (C.I.1, C.I.2, C.II.1-4). EBV LCLs were created from whole blood of A.I.1, A.II.3, C.I.1 and C.II.1-4. The severe clinical condition and heavily immunocompromised condition of patient B.II.1 hindered a blood sample collection for creation of EBV LCLs. A skin biopsy, to create a fibroblast cell line, could be performed in patient A.II.3, carrier A.I.1 and patient B.II.1. Unfortunately, no skin biopsy could be performed in members of family C.

Whole exome sequencing and sanger sequencing.

Whole exome sequencing (WES) was performed for members of family A (A.I.1, A.I.2, A.II.3 and A.II.4), family B (B.I.2 and B.II.1) and the siblings of family C (C.II.1-3), except for C.II.4. **Sanger sequencing** was performed to confirm the identified *COPA* variants. The methods used for genomic DNA preparation, WES analysis and Sanger sequencing are described in the Supplemental Methods.

Patients' cells, (primary) immortalized cell lines and cell culture.

Isolation of peripheral blood mononuclear cells (PBMCs) from the blood of patients and healthy donors, creation of primary immortalized cell lines (EBV LCLs and fibroblasts) and cell culture

was performed according to standard methods, as described in the Supplemental Methods.

RNA extraction and qRT-PCR.

The methods used for mRNA isolation and cDNA preparation and qRT-PCR analysis are explained in detail in the Supplemental Methods. A list of used probes is supplied as well (**Supplemental Table 6).**

Western blotting.

Immunoblotting was performed on cell lysates using standard methods as described in the Supplemental Methods; antibodies are listed in the supplemental material **(Supplemental Table 7).**

Plasmids.

The creation and usage of plasmids for overexpression in HEK293T cells is described in detail in the Supplemental Methods.

Cell transfection.

HEK293T cells (ATCC) were seeded in a 24-well plate, 96-well plate (luciferase assay) or in a T25 flask (co-IP), in DMEM medium supplemented with 10% FCS and transfected at 70% confluency. First, for co-transfection of COPA and STING, WT or mutant COPA pCMV6-AN-DDK DNA plasmids were co-transfected with a pMSCV vector encoding STING or EV of STING (17). 200ng of each DNA plasmid was employed using X-tremeGENE 9 DNA Transfection Reagent (Merck). When different ratios of WT and mutant COPA cDNA were cotransfected, the total amount of COPA cDNA was maintained at 400ng. To demonstrate the dominant negative

effect, the fold change of 400ng of WT COPA co-transfected with STING was considered as 100%, 300ng of WT COPA and 100ng of EV of COPA as 75%, 200ng of WT COPA and 200ng of EV of COPA as 50% and 100ng of WT COPA and 300ng of EV of COPA as 25% and 400ng of EV of COPA as 0%. After 24 hours, cells were stimulated with 2'3'-cGAMP. 48 hours after cotransfection cells were harvested and whole cell lysate was prepared or trizol (500µl per well) was added for RNA extraction. Secondly, for the co-IP assay, 1800ng of each plasmid was co-transfected using Lipofectamine 2000 (Invivogen). WT or mutant COPA pCMV6-AN-DDK DNA plasmids were co-transfected with a pCMV6-XL5 and pCMV6-AC plasmid encoding respectively COPB2 and COPE or their EVs.

Co-immunoprecipitation.

48 hours after transfection cells were harvested and whole cell extract was prepared as described above. Extracts were incubated overnight with 1µg of anti-DDK (Flag) monoclonal antibody Origene) (**Supplemental table 7).** The following day, Protein G Magnetic Beads (Surebeads, Biorad) were added . After a 1 hour of incubation, the beads were magnetized using a DynaMag-2 magnet (Invitrogen, Thermo Fisher Scientific) and washed several times with PBS 0.1% Tween 20. Blot LDS Sample Buffer (4X, Novex) was used as an elution buffer and finally denaturation was performed at 95°C for 3 minutes. Concurrent with the immunoblotting of the obtained eluate, a 10th of the amount of the whole cell extract used for the IP was blotted as the input condition. Immunoblotting for Flag-antibody, COPB2 and COPE was performed as described above (**Supplemental table 7**).

Structural modeling.

Structural modeling of COPA and its interaction with COPE was performed as described in the

Supplemental Methods.

Trafficking assays.

All cells were deposited on labtech (Chamber SlideTM system 154534 - ThermoFisher) and cultured at 37°C, 5% CO2 in a humid environment. For the evaluation of the anterograde ER-to-Golgi transport we followed endogenous PCI in fibroblasts. Fibroblasts were incubated for 3h at 40°C in DMEM supplemented with 10 % Fetal Calf Serum, antibiotics (Penicillin and Streptomycin) and sodium pyruvate, and then, shifted them to 32°C for the indicated times. For the evaluation of the retrograde transport (CtxB assay) Alexa Flour 555-labeled Cholera toxin B subunit (CtxB) was obtained from Molecular Probes (C34776). Cells were incubated with 0.15µg/mL CtxB on ice for 30 min. After washing twice with PBS, the cells were incubated with pre-warmed DMEM medium for the indicated times (Time 0 corresponds to 2 hours afterexposure to the Cholera toxin; Time 8 hours thus corresponds to 10 hours of incubation with the Cholera toxin). Cells were fixed with 4 % paraformaldehyde (Electron Microscopy Sciences) for 10 min. Then, they were washed once in saturation buffer [PBS 1 % BSA (Sigma)], permeabilized with Triton 0,1% buffer for 10 minutes and were washed twice in permeabilization buffer (PBS containing 0.1 % saponin (Fluka Biochemika) and 0.2 % BSA). Cells were then incubated for 45 min with the following primary antibodies based on the type of experiment: anti-PC-I, Anti-GM130, Goat anti-SERCA2 ATPase antibody (**Supplemental Table 8**). Cells were then washed twice with 1.5 mL of saponin buffer to remove non-specifically bound antibodies and incubated with secondary antibodies for 30 minutes. Cells were washed twice in saponin buffer and twice with 500 µL of PBS. The labeling of the nuclei was next performedwith 1 µg/mL of Hoechst for 5 min in the dark. Cells were finally washed twice with 1.5 mL PBS, and mounted

with FluorSaveTM Reagent (Millipore). All experiments are representative of at least 3 independent experiments.

Intracellular fluorescent labeling, confocal microscopy and image analysis.

Intracellular fluorescent labeling in HEK293T cells, EBV LCLs, fibroblasts and quantification of the results were performed as described in the Supplemental Methods.

Electron microscopy.

Electron microscopy was performed on fibroblasts of a healthy control and patient A.II.3 as detailed in the Supplemental Methods.

IFN score in patient samples.

To evaluate the IFN score, the mRNA expression of six ISGs (*IFI27, IFI44L, IFIT1, ISG15, RSAD2* and *SIGLEC1*) was evaluated performing RT-qPCR analysis on cDNA, extracted from peripheral blood or PBMCs as described above. The mRNA expression of these ISGs was normalized to the expression level of *GAPDH*. As previously described, the mRNA expression of each of the six ISGs was expressed relative to a single calibrator (51). The median fold change of the six genes compared with the median of 20 previously collected healthy controls was used to create an IFN score for each individual, with an abnormal score defined as >2 SDs above the mean of the control group, i.e. 2.73. For individual A.II.3 several cDNA samples were available and calculation of IFN scores through the disease course was possible.

Cytokine evaluation in serum samples.

Cytokine evaluation in serum was performed as described in the Supplemental Methods.

Flow cytometry.

Flow cytometry methods used for the evaluation of pSTAT1 in PBMCs, CD169/SIGLEC-1 in monocytes and the T helper cell staining are described in detail in the Supplemental Methods. The used antibodies are listed in the Supplemental Methods (**Supplemental Table 7).**

Luciferase assay.

HEK293T cells were seeded into a 96-well plate and co-transfected as described above with 200ng of WT of mutant COPA and 200ng of EV or WT STING. Additionally a luciferase reporter plasmid (100ng, Promega) and a Renilla Luciferase Control Reporter Vector (20ng, Promega) were co-transfected. After 24 hours a positive control was generated through stimulation with IFNα (10 000U/mL, Life Technologies). 36 hours after transfection, the luciferase activity in the total cell lysate was measured.

Evaluation of ER stress in EBV LCLs and fibroblasts.

As previously described, baseline and induced ER stress were evaluated in EBV LCLs (14). ER stress was induced experimentally by stimulation with thapsigargin, an inhibitor of the ER Ca2+ ATPase. 1.10^6 cells/ml were either treated with DMSO, in the unstimulated condition, or with thapsigargin (10µM, Sigma), in the stimulated condition, during 6 hours. Subsequently the mRNA expression of 3 UPR genes *(DDIT3, HSPA5* and *ATF4)* in unstimulated and stimulated conditions was evaluated. For each gene, CT values were normalized to GAPDH and secondly to the mean CT value of the unstimulated healthy control samples. To evaluate BiP intensity in fibroblasts by confocal microscopy, cells were stimulated for 20 hours with thapsigargin

(Thapsi,10μM, Sigma) and fixation, permeabilization and intracellular fluorescent labeling were performed as described in the Supplemental Methods.

NF-κB nuclear translocation in fibroblasts.

Evaluation of NF-κB nuclear translocation in fibroblasts by immunoblotting and confocal microscopy was performed as described in the Supplemental Methods.

Bulk RNA sequencing

Bulk RNA sequencing was performed on RNA isolated from PAX tubes. A detailed description is available in the Supplemental Methods.

Web resources

The URLs for data presented in this paper are as follows: Chromas: https://technelysium.com.au/wp/; Prism: www.graphpad.com; http://broadinstitute.github.io/picard/; Annovar: http://anovar.openbioinformatics.org; Uniprot: https://www.uniprot.org/; Biorender: www.biorender.com

Statistics

All data are presented as mean ± SEM or mean ± SD, as indicated in the figure legends. Statistical significance for single comparisons was calculated using the one-way ANOVA or two-way ANOVA and mixed-effects analysis was used to examine repeated measures. Dunnett's,Šidák's and Tukey's multiple comparisons tests were used to control for multiple comparisons. Statistical significance for multiple comparisons was computed as specified in the figure legends. Analyses were performed with PRISM software (version 9.0.0 for Windows, GraphPad Software, San

Heterozygous mutations in the C-terminal domain of COPA Laboratory of IEI KU Leuven

Diego, California USA) as indicated in the legend of the figures. A p-value of <0.05 was considered significant.

Study approval

This study was approved by the Ethics Committee Research UZ / KU Leuven (protocol number S65153, S63078). All participating individuals or their legal representatives gave written informed consent prior to sample collection and processing. Informed consent was in accordancewith the Declaration of Helsinki.

Data availability

The RNA sequencing data were deposited to the SRA database under the Bioproject ID PRJNA1051072. Source data are provided as Supporting data values, provided with this paper. Reported patients did not consent to share their genetic data on a public database. Additional data can be obtained upon request to the corresponding author.

Author contributions

SD, LM, JD and IM designed this research study. IM, LM and JD supervised. IM, GB and SD provided funding. SD, AI, LM and TB conducted experiments. SD, AI, JD and IM wrote the manuscript. AV and BM provided biomolecular models. CP analyzed data. DL and BB generated RNA sequencing data. MB and SD performed RNA sequencing analysis. SM provided EM facility, PB performed EM. IM, CD, TB, MC, RR, GB, KJ, DM, IC, CC and PD participated in clinical care. AC, KW and WH performed genetic analysis and generated primary cell lines. All authors edited the paper.

Acknowledgments

SD is supported by the Research Foundation-Flanders personal grant 11F4421N. AI is supported by an International PhD fellowship from the Université Paris Cité and an ESID fellowship. JD is supported by Inserm and *Agence Nationale de la Recherche* (ANR-19-CE17-0011 RIDES). IM is a Senior Clinical Investigator at the Research Foundation – Flanders, and is supported by a KU Leuven C1 Grant [grant number C16/18/007]; by a VIB GC PID Grant; by the Research Foundation - Flanders (FWO) [grant numbers G0C8517N, G0B5120N and G0E8420N] and by the Jeffrey Modell Foundation. This project has received funding from the European Research Council (ERC) under the European Union's Horizon 2020 research and innovation programme (grant agreement No. 948959). This work was supported by ERN-RITA and by a UZ Leuven KOOR Fonds Academische Studies grant to GB. RS is a FWO senior clinical investigator fellow (1805518N). Further, we would like to acknowledge Ana Kolicheski, PhD, for technical assistance, The Jeffrey Modell Diagnostic and Research Center at St. Louis Children's Hospital, and The Center for Pediatric Immunology at St. Louis Children's Hospital and Washington University in St. Louis. Figure 2A and the graphical abstract were created with Biorender.com (AF26786S56, BA26789KZJ,).

References

1. H H Quek VTC. Genomic organization and mapping of the human HEP-COP gene (COPA) to 1q. *Cytogenet Cell Genet* 1997;76(3–4):139–43.

2. Serafini T et al. A coat subunit of Golgi-derived non-clathrin-coated vesicles with homology to the clathrin-coated vesicle coat protein β-adaptin. *Nature* 1991;349(6306):215–220.

3. M. Gerard Waters TS& JER. "Coatomer": a cytosolic protein complex containing subunits of non-clathrin-coated Golgi transport vesicles. *Nature* 1991;349:248–251.

4. Uhlén M et al. Tissue-based map of the human proteome. *Science.* 2015;347(6220).

5. Uhlen M et al. A genome-wide transcriptomic analysis of protein-coding genes in human blood cells. *Science.* 2019;366(6472).

6. Lowe M, Kreis TE. In vivo assembly of coatomer, the COP-I coat precursor. *J. Biol. Chem.* 1996;271(48):30725–30730.

7. Helms JB, Rothman JE. Inhibition by brefeldin a of a Golgi membrane enzyme that catalyses exchange of guanine nucleotide bound to ARF. *Nature* 1992;360(6402):352–354.

8. Donaldson JG, Cassel D, Kahn RA, Klausner RD. ADP-ribosylation factor, a small GTP-binding protein, is required for binding of the coatomer protein β-COP to Golgi membranes. *Proc. Natl. Acad. Sci. U. S. A.* 1992;89(14):6408–6412.

9. Stenbeck G et al. β'-COP, a novel subunit of coatomer. *EMBO J.* 1993;12(7):2841–2845.

10. Duden R. ER-to-Golgi transport : COP I and COP II function (Review). *Mol. Membr. Biol.* 2003;20(3):197–207.

11. Orci L, Glick BS, Rothman JE. A new type of coated vesicular carrier that appears not to contain clathrin: Its possible role in protein transport within the Golgi stack. *Cell* 1986;46(2):171–184.

12. Barlowe C et al. COPII: A membrane coat formed by Sec proteins that drive vesicle budding from the endoplasmic reticulum. *Cell* 1994;77(6):895–907.

13. Razi M, Chan EYW, Tooze SA. Early endosomes and endosomal coatomer are required for Autophagy. *J. Cell Biol.* 2009;185(2):305–321.

14. Zhang J et al. Aster‐C coordinates with COP I vesicles to regulate lysosomal trafficking and activation of mTORC1. *EMBO Rep.* 2020;21(9):1–18.

15. Watkin LB et al. COPA mutations impair ER-Golgi transport and cause hereditary

autoimmune-mediated lung disease and arthritis. *Nat. Genet.* 2015;47(6):654–660.

16. Vece TJ et al. Copa Syndrome: a Novel Autosomal Dominant Immune Dysregulatory Disease. *J. Clin. Immunol.* 2016;36(4):377–387.

17. Lepelley A et al. Mutations in COPA lead to abnormal trafficking of STING to the Golgi and interferon signaling. *J. Exp. Med.* 2020;217(11).

18. Krutzke S, Rietschel C, Horneff G. Baricitinib in therapy of COPA syndrome in a 15-year-old girl. *Eur. J. Rheumatol.* 2020;7(1):78–81.

19. Zeng J, Hao J, Zhou W, Zhou Z, Miao H. A Novel Mutation c.841C>T in COPA Syndrome of an 11-Year-Old Boy: A Case Report and Short Literature Review. *Front. Pediatr.* 2021;9:1–6.

20. Taveira-Dasilva AM et al. Expanding the phenotype of COPA syndrome: A kindred with typical and atypical features. *J. Med. Genet.* 2018;778–782.

21. Brennan M, Mcdougall C, Walsh J, Crow YJ, Davidson J. A Case report: Copa mutation – a new condition to consider with polyarthritis and interstitial lung disease. *Archives of Disease in Childhood*. 2017;102:167-168.

22. Volpi S et al. Type I interferon pathway activation in COPA syndrome. *Clin. Immunol.* 2018;187:33–36.

23. Noorelahi R. Imaging findings of Copa syndrome in a 12-year-old boy. *Pediatr Radiol* 2018;48:279–282.

24. Cabrera-Pérez JS et al. A Zebra at the Rodeo: Dyspnea, Hematuria, and a Family History of Arthritis. In: *Arthritis Care and Research*. John Wiley and Sons Inc; 2022:165–170

25. Kato T et al. Augmentation of Stimulator of Interferon Genes–Induced Type I Interferon Production in COPA Syndrome. *Arthritis Rheumatol.* 2021;73(11):2105–2115.

26. Guan, Yuhong;Liu, Hui;Tang, Xiaolei;Xu H. Effective sirolimus treatment of 2 COPA syndrome patients. *Artic. CCCCG J. allergy Clin. Immunol. Pract.* 2021;9(2):0–13.

27. Frémond ML et al. Use of ruxolitinib in COPA syndrome manifesting as life-threatening alveolar haemorrhage. *Thorax* 2020;75(1):92–95.

28. Jensson BO et al. COPA syndrome in an Icelandic family caused by a recurrent missense mutation in COPA. *BMC Med. Genet.* 2017;18(129):1–5.

29. Ayyar A, Seaman RD, Guntupalli K, Tolcher MC. Case Report Management of a Novel Autoimmune Disease, COPA Syndrome, in Pregnancy. *Case Rep. Obstet. Gynecol.* 2022;6–9.

30. Riddell P et al. IL-6 receptor blockade for allograft dysfunction after lung transplantation in a patient with COPA syndrome. *Clin. Transl. Immunol.* 2021;10:1–7.

31. This H, Rice GI. Rheumatoid factor positive polyarticular juvenile idiopathic arthritis associated with a novel COPA mutation. *Rheumatology* 2021;171–173.

32. Thaivalappil SS, Garrod AS, Borowitz SM, Watkin LB, Lawrence MG. Persistent Unexplained Transaminitis in COPA Syndrome. *J. Clin. Immunol.* 2021;41(1):205–208.

33. Psarianos P et al. COPA Syndrome (Ala239Pro) Presenting with Isolated Follicular Bronchiolitis in Early Childhood: Case Report. *J. Clin. Immunol.* 2021;41(7):1660–1663.

34. Deng Z et al. A defect in COPI-mediated transport of STING causes immune dysregulation in COPA syndrome. *J Exp Med.* 2020; 217(11):e20201045.

35. Mukai K et al. Homeostatic regulation of STING by retrograde membrane traffic to the ER. *Nat. Commun.* 2021;12(1).

36. Steiner A et al. Deficiency in coatomer complex I causes aberrant activation of STING signalling. *Nat. Commun.* 2022;13(1):2321.

37. Taguchi T, Mukai K, Takaya E, Shindo R. STING Operation at the ER/Golgi Interface. *Front. Immunol.* 2021;12:8–13.

38. Eugster A, Frigerio G, Dale M, Duden R. COP I domains required for coatomer integrity , and novel interactions with ARF and ARF-GAP2000;19(15):3905–3917.

39. Travis SM, Kokona B, Fairman R, Hughson FM. Roles of singleton tryptophan motifs in COPI coat stability and vesicle tethering. *Proc. Natl. Acad. Sci. U. S. A.* 2019;116(48):24031–24040.

40. Tagaya M, Arasaki K, Inoue H, Kimura H. Moonlighting functions of the NRZ (mammalian Dsl1) complex. *Front. Cell Dev. Biol.* 2014;2:1–9.

41. Duden R, Kajikawa L, Wuestehube L, Schekman R. ε-COP is a structural component of coatomer that functions to stabilize α-COP. *EMBO J.* 1998;17(4):985–995.

42. Tosato F et al. Lymphocytes subsets reference values in childhood. *Cytom. Part A* 2015;87(1):81–85.

43. Meyts I et al. Exome and genome sequencing for inborn errors of immunity. *J. Allergy Clin. Immunol.* 2016;138(4):957–969.

44. Karczewski KJ et al. The mutational constraint spectrum quantified from variation in 141,456 humans. *Nature* 2020;581(7809):434–443.

45. Sherry ST et al. DbSNP: The NCBI database of genetic variation. *Nucleic Acids Res.* 2001;29(1):308–311.

46. Rentzsch P, Witten D, Cooper GM, Shendure J, Kircher M. CADD: Predicting the deleteriousness of variants throughout the human genome. *Nucleic Acids Res.* 2019;47(D1):D886–D894.

47. Marom R et al. COPB2 loss of function causes a coatopathy with osteoporosis and

developmental delay. *Am. J. Hum. Genet.* 2021;108(9):1710–1724.

48. Venditti R et al. Sedlin controls the ER export of procollagen by regulating the Sar1 cycle. *Science.*. 2012;337(6102):1668–1672.

49. Stephens DJ, Pepperkok R. Imaging of procollagen transport reveals COPI-dependent cargo sorting during ER-to-Golgi transportin mammalian cells. *J. Cell Sci.* 2001;115:1149–1160.

50. Sugawara T et al. PKCδ and ε regulate the morphological integrity of the ER-Golgi intermediate compartment (ERGIC) but not the anterograde and retrograde transports via the Golgi apparatus. *Biochim Biophys Acta*. 2012. 1823(4):861-75.

51. Rice GI et al. Assessment of Type I Interferon Signaling in Pediatric Inflammatory Disease. *J. Clin. Immunol.* 2017;37(2):123–132.

52. Sprooten J, Garg AD. Type I interferons and endoplasmic reticulum stress in health and disease. *Int. Rev. Cell Mol. Biol.* 2020;350:63–118.

53. Kim H et al. Development of a Validated Interferon Score Using NanoString Technology. *J. Interf. Cytokine Res.* 2018;38(4):171–185.

54. Anderson E, Hatch J, Cardinal J, Langguth D, Coman D. Behçet Disease-Like Symptoms with a Novel COPA Mutation . *Case Rep. Genet.* 2020;2020:1–4.

55. Lin L, Fan H, Zhang D, Lu G. Talaromyces marneffei infection associated with bronchiolitis obliterans in an HIV-negative child: a case report. *BMC Infect. Dis.* 2022;22(1).

56. Arakel EC, Schwappach B. Formation of COPI-coated vesicles at a glance. *J. Cell Sci.* 2018;131(7).

57. Szul T, Sztul E. COPII and COPI traffic at the ER-Golgi interface. *Physiology* 2011;26(5):348–364.

58. Nihira H et al. Detailed analysis of Japanese patients with adenosine deaminase 2 deficiency

reveals characteristic elevation of type II interferon signature and STAT1 hyperactivation. *J. Allergy Clin. Immunol.* 2021;148(2):550–562.

59. Rivara S, Ablasser A. COPA silences STING. *J. Exp. Med.* 2020;217(11):3–5.

60. Li A, Song NJ, Riesenberg BP, Li Z. The Emerging Roles of Endoplasmic Reticulum Stress in Balancing Immunity and Tolerance in Health and Diseases: Mechanisms and Opportunities. *Front. Immunol.* 2020;10:1–15.

61. Dell'Angelica EC, Bonifacino JS. Coatopathies: Genetic disorders of protein coats. *Annu. Rev. Cell Dev. Biol.* 2019;35:131–168.

62. Izumi K et al. ARCN1 Mutations Cause a Recognizable Craniofacial Syndrome Due to COPI-Mediated Transport Defects. *Am. J. Hum. Genet.* 2016;99(2):451–459.

63. Bainter W et al. Combined immunodeficiency due to a mutation in the γ1 subunit of the coat protein I complex. *J. Clin. Invest.* 2021;131(3):1–17.

64. Ren J, Bi Y, Sowers JR, Hetz C, Zhang Y. Endoplasmic reticulum stress and unfolded protein response in cardiovascular diseases. *Nat. Rev. Cardiol.* 2021;18(7):499–521.

65. Claerhout S et al. Abortive autophagy induces endoplasmic reticulum stress and cell death in cancer cells. *PLoS One.* 2012;7(6).

Legends figures

Figure 1. **Three heterozygous mutations in the C-terminal domain of COPA in six patients with an autoinflammatory and autoimmune phenotype.**

(A) Pedigrees of the families A, B and C with indication of the genotype, assigned with the amino acid changes, below each individual. Affected individuals are indicated by black filled symbols and an arrow, gray half-filled symbols indicate unaffected heterozygous carriers and open shapes indicate unaffected family members. Squares designate males and circles females. Patient 2 (B.II.1) succumbed at the age of 7 years old due to HLH and MOF. Patient 5 (C.II.3) and 6 (C.II.4) are dizygotic twins. Sanger sequencing chromatograms for *COPA*, performed on genomic DNA, are shown, covering a 15 bp snapshot around the mutation. Red arrows indicate the position of the mutation. **(B)** Medical imaging for patient 1 (A.II.3). Brain magnetic resonance imaging (MRI, T2 weighted images) shows a hyperintense optic chiasm (red arrow), indicative for neuromyelitis optica with involvement of the optic chiasm (upper left panel). Spinal cord MRI illustrates (T2 weighted images) a swollen spinal cord with central hyperintensity (red bracket), ranging from the level of cervical vertebra 4 (C4) till thoracic vertebra 8 (T8), revealing transverse myelitis (lower left panel). Chest computed tomography (CT) demonstrates bronchiectasis (right upper panel) and MRI of the abdomen depicts hepatosplenomegaly (right lower panel, red arrows). **(C)** Chest CT of patient 2 (B.II.1) shows signs of an alveolar hemorrhage and centrilobular nodules.

Figure 2. **Genetic aspects and in silico pathogenicity prediction of mutations in the CTD of COPA .**

(A) Schematic illustration of the COPA protein and its domains. Previously reported mutations in the WD40 domain are depicted in black (full circle functionally validated, blank circle functional validation unavailable), mutations in the CTD of COPA are depicted in color (color code correlates with **Figure 1A**). Numbers in brackets refer to the number of families identified, number of mutation carriers and number of diseased, respectively. Coatomer WDAD, coatomer WD-associated region. **(B)** Population genetics of the previously described *COPA* mutations affecting the WD40 domain, the previously published not functionally validated CTD mutations and the CTD COPA mutations. MAF, minor allele frequency; MSC, mutation significance cutoff; CADD, combined annotation-dependent depletion score. **(C)** Conserved sequence homology at the site of the identified mutations in distantly related eukaryotes. **(D)** Biomodelling of the mutations affecting the CTD of COPA. The central figure depicts the main proteins of COPI, COPA (orange), COPB (teal), COPB2 (blue), COPE (purple). On the left, the physical interaction between $COPA^{R1142X}$ and $COPA^{WT}$ is depicted. In the upper representation, $COPA^{WT}$ is shown as surface and $COPA^{R1142X}$ as a cartoon inside the surface, illustrating the complete removal of the dimerization interface of $COPA^{R1142X}$ with the neighboring $COPA^{WT}$ (circle). This exposes the hydrophobic interface of the COPE binding helices thus disrupting the COPA-COPE dimer. In the lower representation, the absent residues are colored in gray. On the right, the interaction between $COPA^{R1058C}$, $COPA^{C1013S}$ and COPE is shown. $COPA^{R1058C}$ and $COPA^{C1013S}$ likely disturb the conformation of the α-helices on which they are located and subsequently disrupt COPA's overall structure. **(E)** Magnification of biomodelling of the α-helices, which compose the main body of the

CTD and comprise residues 1013 and 1058, and form a binding site for singleton tryptophan motif (STM). STM are known to be crucial for COPA homo-oligomerization and ER-tethering of COPI vesicles.

Figure 3. **Analysis of COPA, COPB2 and COPE mRNA and protein expression in patients affected by mutations in the CTD of COPA.**

(A-B) RT-qPCR analysis of transcript levels of *COPA, COPB2* and *COPE* analyzed in cDNA extracted from whole blood (for patients and carriers of family A and C) or PBMCs (for B.I.2 and B.II.1). Panel A demonstrates *COPA* mRNA expression, evaluated using 4 probes covering exon 2-3, exon 4-5, exon 11 and exon 32-33. In panel B, transcripts levels of *COPA* (calculated as the mean of the transcript levels of the 4 COPA probes, shown in panel A), *COPB2* and *COPE* are shown. The relative mRNA level depicts the fold increase of the gene expression normalized to GAPDH (ΔCT) and to the mean ΔCT of the control samples. 3-4 samples from separate time points were analyzed for A.II.3 and A.I.1. **(C)** Western blot analysis of COPA, COPB2 and COPE in whole cell lysates of PBMCs of A.I.1, A.II.3 and 3 healthy controls. Immunoblotting of COPA with an antibody specific for the N-terminal region of COPA (N-COPA) and an antibody specific for the C-terminal region of COPA (C-COPA). **(D)** Quantification of protein level of COPA, detected by N-COPA and C-COPA antibody (left panel), and COPB2 and COPE (right panel), as observed in C. Band intensity was determined relative to GAPDH and normalized to the mean of the healthy controls (n=8, 5 adults, 3 children). **(E)** Western blot analysis of COPA, COPB2 and COPE in EBV LCLs of A.I.1, A.II.3, C.I.1 and C.II.1-4 in comparison with 4 adult healthy controls. **(F)** Western blot analysis of COPA, COPB2 and COPE in fibroblasts of A.I.1 and A.II.3, and B.II.1 in comparison with 2 healthy controls. Results in C-F are representative for 2-3

independent experiments. For A, B and D, columns and bars represent mean ± SEM values, statistically analyzed using two-way ANOVA (*, P<0.05; **, P<0.01; ***, P<0.001; ****, P<0.0001).

Figure 4. **COPA^{R1142X} and COPA^{R1058C} disrupt COPI integrity and impair anterograde ER-to-Golgi and retrograde Golgi-to-ER trafficking.**

(A) Western blot analysis of FLAG, N-terminal COPA, COPB2, COPE and β-actin antibody in whole cell extract (input) or eluate of IP of HEK293T cells co-transfected with both WT or mutant COPA and WT or EV of COPB2 and COPE. Immunoprecipitation was performedwith an antibody against FLAG (IP COPA). **(B)** Quantification of COPB2 and COPE protein levels co-immunoprecipitated with COPA-Flag (COPA IP) compared to the input signal, as observed in A. **(C)** Immunofluorescence analysis of PCI transport assay in 4 different control fibroblasts (one representative control is shown), COPA^{R1142X} fibroblasts, derived from A.I.1 and A.II.3, and COPA^{R1058C} fibroblasts, derived from B.II.1, at 0 min and 60 min. Scale bar 10 µm. **(D)** Graphs represent the quantification of the ER exit (upper panel) and Golgi entry (lower panel) of PCI, as shown in C. **(E)** Immunofluorescence analysis of CtxB transport assay in 4 different control fibroblasts, COPA^{R1142X} fibroblasts, derived from A.I.1 and A.II.3, and COPA^{R1058C} fibroblasts, derived from B.II.1. Analysis was performed 2 hours and 10 hours after the exposure to the CtxB. Scale bar 10 µm. **(F)** Graphs represent the quantification of the Golgi release (upper panel) and ER entry (lower panel) of CtxB, as observed in E. In panel B, D and F results are shown as mean +/- SEM and the significance levels were calculated using one (in D and F) or two (in B) way ANOVA (*, P<0.05; **, P<0.01; ***, P<0.001; ****, P<0.0001). Data are representative for 2-3 independent experiments. **(G)** Electron microscopy of COPA^{R1142X} fibroblasts, derived from

A.II.3, compared to fibroblasts from a healthy control. Magnification 15 000, scale bar 200nm. The images demonstrate a fragmented and disorganized Golgi apparatus (blue box) and an accumulation of vesicles (red box) in the cytosol of $COPA^{R1142X}$ fibroblasts (blue box).

Figure 5. **Mutations in the CTD of COPA induce type 1 IFN pathway activation in 3 out of 6 patients.**

(A) IFN scores (left panel) and ISG expression (right panel) in peripheral whole blood of patients and their families. mRNA expression of the individual ISGs (right panel) for three healthy controls, one IFN-α and IFN-β stimulated PBMC sample of a healthy control, one SAVI patient (carrying a p.V155M mutation in *STING*), one AGS patient (heterozygous for a p.S962A fs*92 and a p.P193A mutation in *ADAR)* and the patients, carriers and healthy family members included in the left panel. The first number in brackets is the decimalized age at the time of sampling, the second the IFN score. Mean ± SEM values of different time points, if available, are shown (n=7 for A.II.3 (prior to transplantation); n=3 for A.I.1, A.I.2, A.II.4; n=2 for A.II.2 and n=1 for other individuals). **(B)** Evolution of type I IFN score (left) and CRP value (right) through the disease course of patient A.II.3. Timing is indicated in days prior to hematopoietic stem cell transplantation. Relevant clinical manifestations and treatments are indicated. **(C)** Flow cytometry analysis of pSTAT1 in monocytes of A.II.3 compared with a control and a STAT1 GOF patient. The ratio of the amount of pSTAT1 positive cells in comparison to the unstimulated condition is indicated. Data are representative for two independent experiments. **(D)** Immunofluorescent analysis of STING localization in fibroblasts (upper panel) and EBV LCLs (bottom panel) of healthy controls, A.I.1, A.II.3, B.II.1, C.I.1 and C.II.1-4. Cells were stained for STING-TMEM173, cis-Golgi (Giantin) and nucleus (Hoechst). The merge column represents an overlay

between the stains. Scale bar 10µm. **(E)** Quantification of the colocalization of STING and cis-Golgi, expressed as the PC. Results are representative of at least 3 independent experiments. Results are shown as means +/- SEM and the significance levels were calculated using one-way ANOVA (*, P<0.05; **, P<0.01; ***, P<0.001; ****, P<0.0001).

Figure 6**. Overexpression of the CTD COPA mutants does not induce STING-dependent type I IFN signaling in HEK293T cells.**

For panels A-F, HEK293T cells were co-transfected with EV or WT STING and WT or mutant COPA as indicated. **(A)** Immunoblotting of whole-cell lysates for COPA (Flag), p-IRF3, total IRF3, STING and β-actin. **(B)** Quantification of p-IRF3 protein relative to total IRF3, as demonstrated in A. **(C) Relative** mRNA expression of *IFIT1* and *ISG15*, normalized to GAPDH and to HEK293T cells expressing COPA EV and STING EV. First, expression was compared between cells co-transfected with STING and $COPA^{WT}$ and cells co-transfected with STING and mutant COPA (lines and asterisk). Secondly, expression in cells co-transfected with STING EV and WT or mutant COPA was compared to the corresponding condition co-transfected with STING (asterisks above error bars). Cells stimulated with 2'3'-c-GAMP served as a positive control. **(D)** ISRE-luciferase reporter assay. Luciferase activity was measured in total cell lysate. **(E)** Confocal microscopy of COPA and STING co-localization. Cells were stained for COPA (Flag), STING, Golgi (GM130) and ER (Calnexin). The additional square in the STING column contains an enlargement of the image. Scale bar, 25µm. **(F)** Quantification of the ratio of STING localized to the Golgi over total STING, as demonstrated in E. Results in A-F, are representative for 2-4 independent experiments. For B-D and F, columns and bars represent mean ± SEM, analyzed using one-way (F) or two-way (B-D) ANOVA (*, P<0.05; **, P<0.01;). **(G)** Relative

mRNA expression of *IFIT1* in HEK293T cells co-transfected with different ratios of WT and mutant COPA and EV or WT STING. The triangle depicts the amount of transfected WT, EV or mutant COPA cDNA. Dashed lines and the right y-axis illustrate the fold change of *IFIT1* corresponding to HEK293T cells co-transfected with different percentages of WT COPA Variants are classified based on their effect on *IFIT1* expression. The mean of three technical replicates is shown.

Figure 7. **CTD COPA mutations cause activation of ER stress and pro-inflammatory signaling pathways such as the NF-κB pathway.**

(A) Relative mRNA expression of *HSPA5*, *ATF4*, *DDIT3* and *COPA* in EBV LCLs of 4 healthy controls, A.I.1, A.II.3, C.I.1 and C.II.1-4. LCLs were unstimulated (white; -) or treated for 6 hours with thapsigargin (black; +). Results were normalized to GAPDH (ΔCT) and to the control samples (ΔΔCT). **(B)** Representative images of immunofluorescent analysis of BiP intensity in fibroblasts of healthy controls, A.I.1, A.II.3 and B.II.1. Cells were stained for BiP, F-actin and nucleus and stimulated with thapsigargin. Graphs represent the quantification of the MFI of BiP. **(C)** Representative images of immunofluorescent analysis of p65-NF-κB nuclear translocation in fibroblasts of healthy controls, A.I.1, A.II.3 and B.II.1. Cells were stimulated with LPS and stained for p65-NF-κB and nucleus. Nuclear translocation of p65 appears violet. Graphs represent the quantification of the nuclear translocation of NF-κB. Scale bar, 10μm. For A-C, columns and bars represent mean ± SEM, representative of two (A) to three (B-C) independent experiments. Statistical analysis was performed using one (A) or two-way ANOVA (B-C) (*, P<0.05; **, P<0.01; ***, P<0.001; ****, P<0.0001). Panels D-F represent the analysis of bulk RNA sequencing data of whole blood RNA of 4 controls (black), 2 carriers (A.I.1 and C.I.1), 1 SAVI patient (green) and 5

patients (A.II.3 , C.II.1-4)**. (D)** PCA plot of bulk RNA sequencing data, based on the 1000 genes with the largest intersample variance (after a variance stabilizing transformation removing the variance dependence on the mean). **(E)** Top 10 differentially expressed pathways determined by IPA analysis of the differential gene expression for patient A.II.3 (left panel) and C.II.4 (right panel) versus the group consisting of the carriers (A.I.1, C.I.1), controls, SAVI patient and C.II.1-3. **(F)** Heatmaps represent the differential expression analysis for the eIF2 pathway, for 24 autophagy genes and a limited list of ISGs.

Figure 1

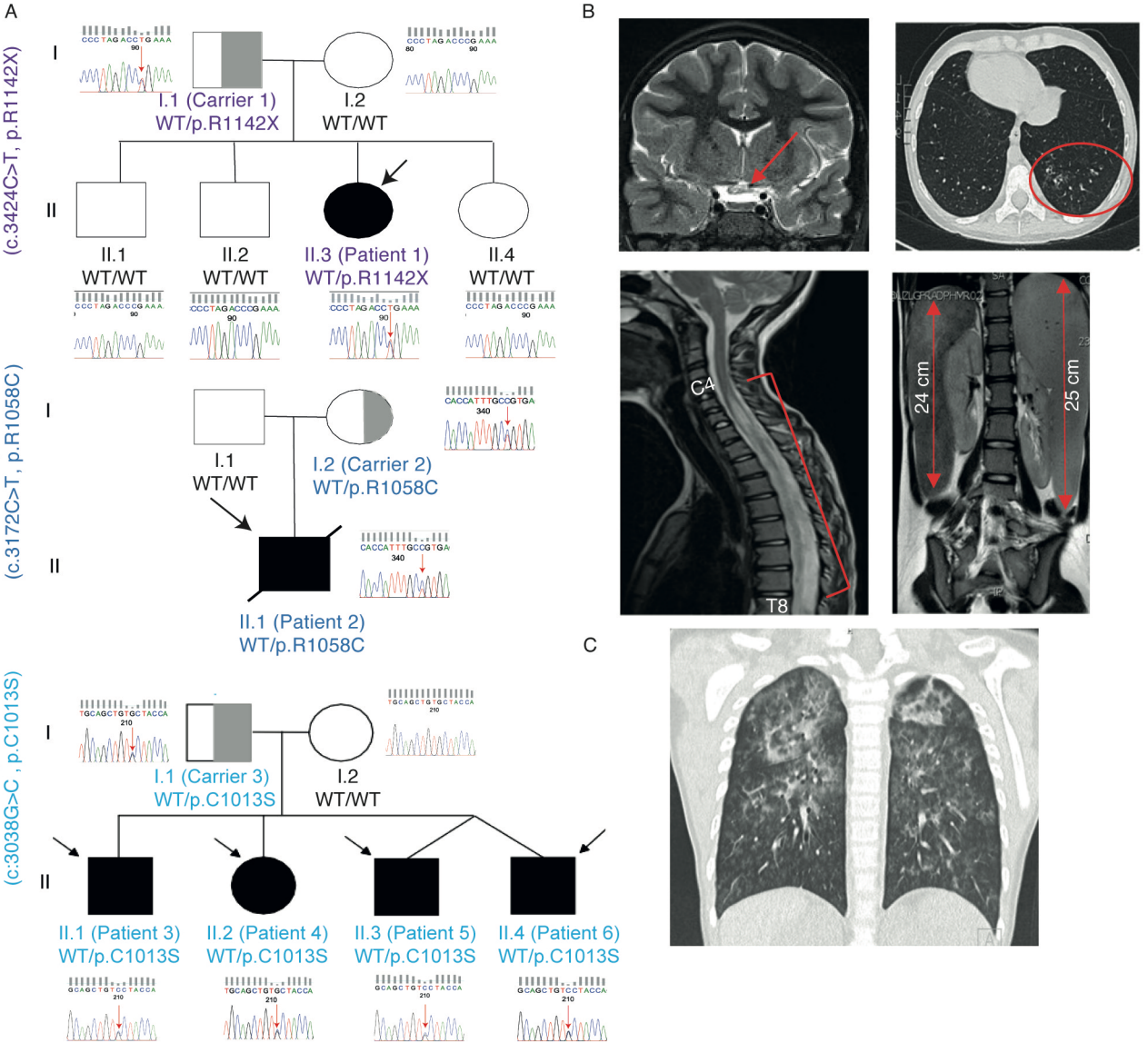
A
Family A
(c.3424C>T, p.R1142X)
I
I.1 (Carrier 1)
WT/p.R1142X
I.2
WT/WT
II
II.1
WT/WT
II.2
WT/WT
II.3 (Patient 1)
WT/p.R1142X
II.4
WT/WT
Family B
(c.3172C>T, p.R1058C)
I
I.1
WT/WT
I.2 (Carrier 2)
WT/p.R1058C
II
II.1 (Patient 2)
WT/p.R1058C
Family C
(c:3038G>C , p.C1013S)
I
I.1 (Carrier 3)
WT/p.C1013S
I.2
WT/WT
II
II.1 (Patient 3)
WT/p.C1013S
II.2 (Patient 4)
WT/p.C1013S
II.3 (Patient 5)
WT/p.C1013S
II.4 (Patient 6)
WT/p.C1013S
B
C4
T8
24 cm
25 cm
C

Figure 2

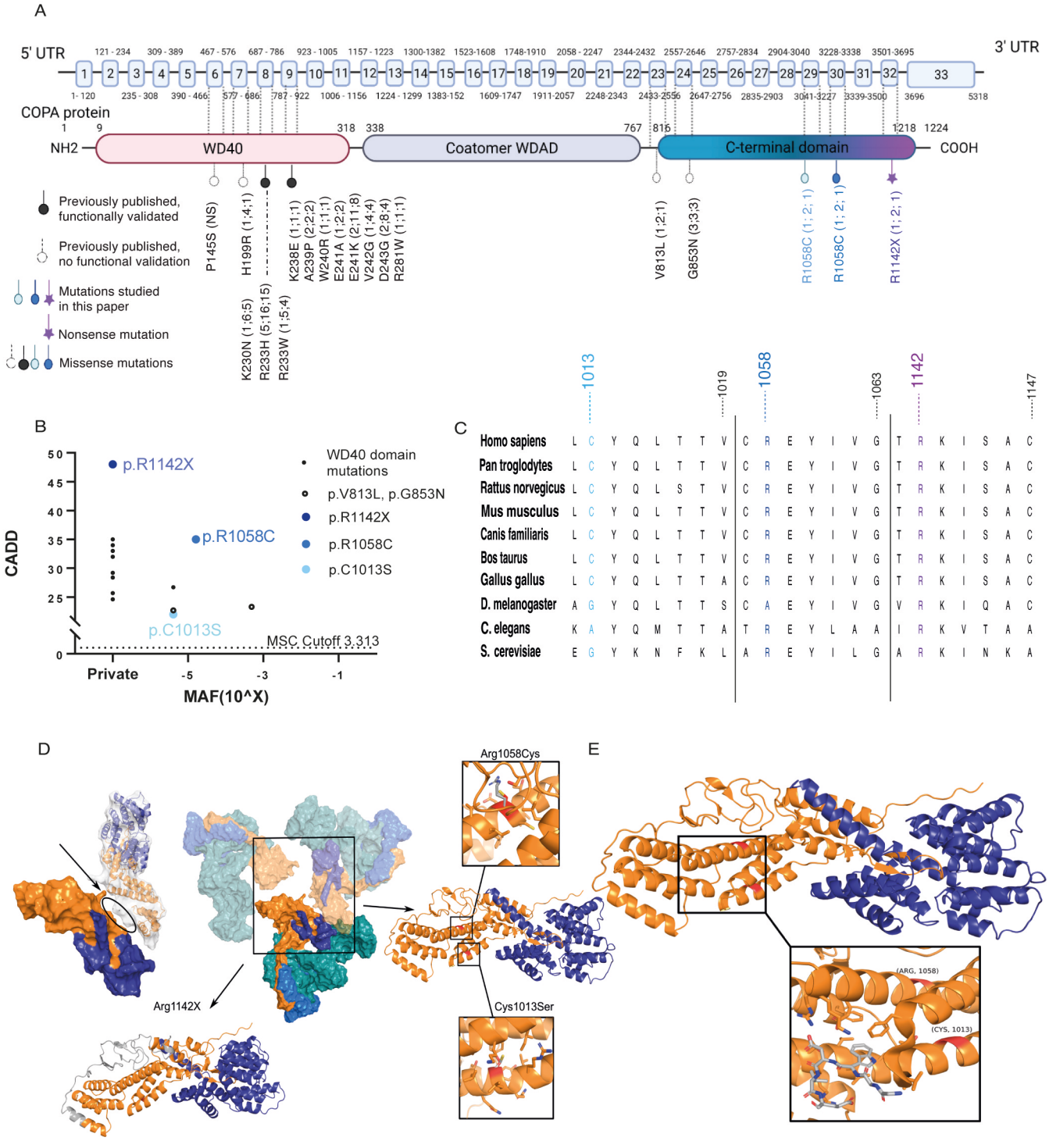
A
5' UTR
3' UTR
COPA protein
NH2
WD40
Coatomer WDAD
C-terminal domain
COOH
Previously published, functionally validated
Previously published, no functional validation
Mutations studied in this paper
Nonsense mutation
Missense mutations
P145S (NS)
H199R (1;4;1)
K230N (1;6;5)
R233H (5;16;15)
R233W (1;5;4)
K238E (1;1;1)
A239P (2;2;2)
W240R (1;1;1)
E241A (1;2;2)
E241K (2;11;8)
V242G (1;4;4)
D243G (2;8;4)
R281W (1;1;1)
V813L (1;2;1)
G853N (3;3;3)
R1058C (1; 2; 1)
R1058C (1; 2; 1)
R1142X (1; 2; 1)
B
CADD
MAF(10^X)
p.R1142X
p.R1058C
p.C1013S
WD40 domain mutations
p.V813L, p.G853N
p.R1142X
p.R1058C
p.C1013S
MSC Cutoff 3.313
Private
C
Homo sapiens
Pan troglodytes
Rattus norvegicus
Mus musculus
Canis familiaris
Bos taurus
Gallus gallus
D. melanogaster
C. elegans
S. cerevisiae
D
Arg1058Cys
Arg1142X
Cys1013Ser
E
(ARG, 1058)
(CYS, 1013)

Figure 3

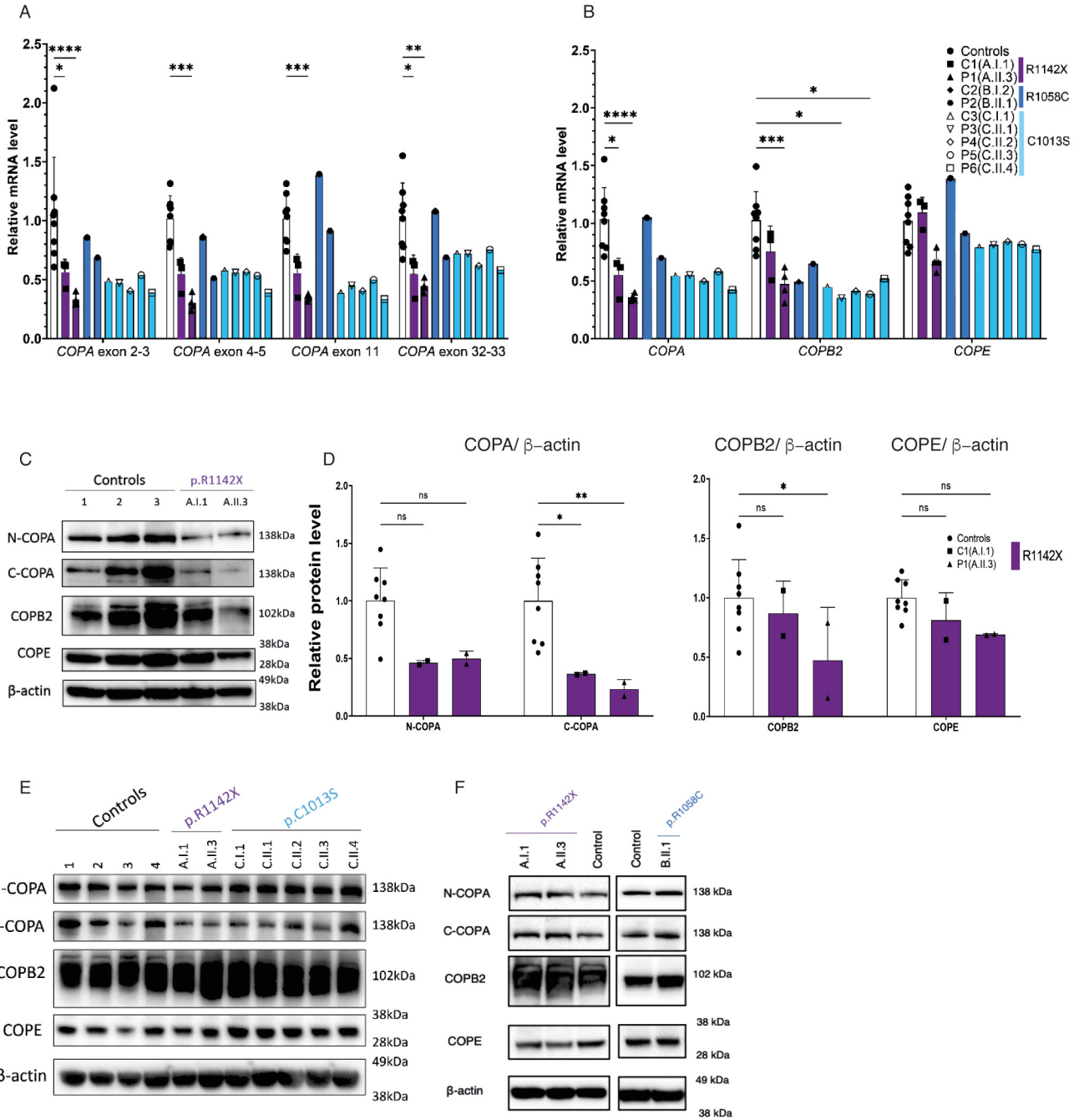
A
Relative mRNA level
COPA exon 2-3
COPA exon 4-5
COPA exon 11
COPA exon 32-33
B
Relative mRNA level
COPA
COPB2
COPE
Controls
C1(A.I.1)
P1(A.II.3)
C2(B.I.2)
P2(B.II.1)
C3(C.I.1)
P3(C.II.1)
P4(C.II.2)
P5(C.II.3)
P6(C.II.4)
R1142X
R1058C
C1013S
C
Controls
p.R1142X
1
2
3
A.I.1
A.II.3
N-COPA
C-COPA
COPB2
COPE
β-actin
138kDa
138kDa
102kDa
38kDa
28kDa
49kDa
38kDa
D
COPA/ β−actin
COPB2/ β−actin
COPE/ β−actin
Relative protein level
N-COPA
C-COPA
COPB2
COPE
ns
Controls
C1(A.I.1)
P1(A.II.3)
R1142X
E
Controls
p.R1142X
p.C1013S
1
2
3
4
A.I.1
A.II.3
C.I.1
C.II.1
C.II.2
C.II.3
C.II.4
N-COPA
C-COPA
COPB2
COPE
β-actin
138kDa
138kDa
102kDa
38kDa
28kDa
49kDa
38kDa
F
p.R1142X
p.R1058C
A.I.1
A.II.3
Control
Control
B.II.1
N-COPA
C-COPA
COPB2
COPE
β-actin
138 kDa
138 kDa
102 kDa
38 kDa
28 kDa
49 kDa
38 kDa

Figure 4

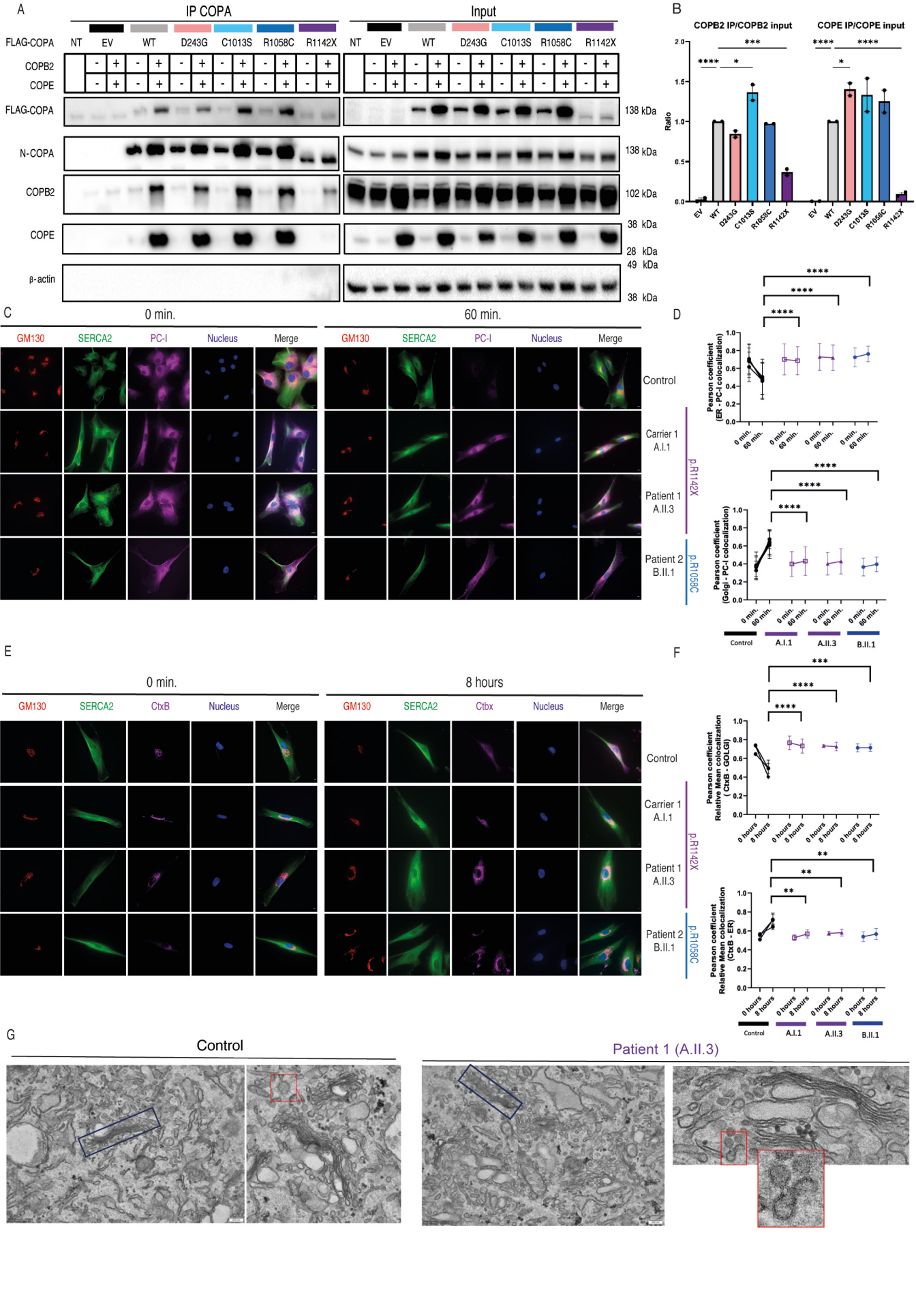
A
IP COPA
Input
FLAG-COPA
NT
EV
WT
D243G
C1013S
R1058C
R1142X
COPB2
COPE
FLAG-COPA
N-COPA
COPB2
COPE
β-actin
138 kDa
138 kDa
102 kDa
38 kDa
28 kDa
49 kDa
38 kDa
B
COPB2 IP/COPB2 input
COPE IP/COPE input
Ratio
C
0 min.
60 min.
GM130
SERCA2
PC-I
Nucleus
Merge
Control
Carrier 1 A.I.1
Patient 1 A.II.3
Patient 2 B.II.1
p.R1142X
p.R1058C
D
Pearson coefficient (ER - PC-I colocalization)
Pearson coefficient (Golgi - PC-I colocalization)
0 min.
60 min.
Control
A.I.1
A.II.3
B.II.1
E
0 min.
8 hours
GM130
SERCA2
CtxB
Ctbx
Nucleus
Merge
Control
Carrier 1 A.I.1
Patient 1 A.II.3
Patient 2 B.II.1
p.R1142X
p.R1058C
F
Pearson coefficient Relative Mean colocalization (CtxB - GOLGI)
Pearson coefficient Relative Mean colocalization (CtxB - ER)
0 hours
8 hours
Control
A.I.1
A.II.3
B.II.1
G
Control
Patient 1 (A.II.3)

Figure 5

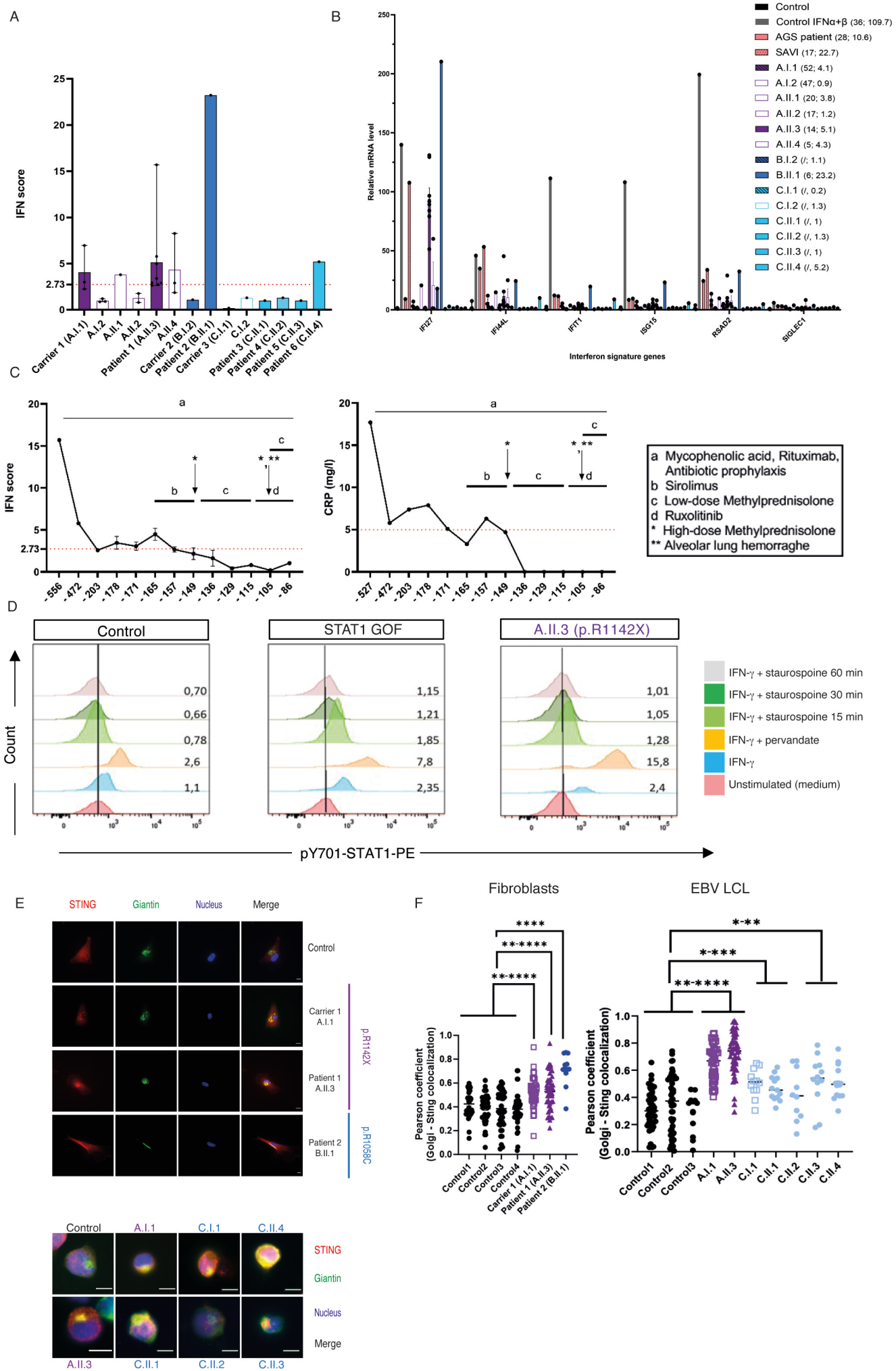
A
IFN score
Carrier 1 (A.I.1)
A.I.2
A.II.1
A.II.2
Patient 1 (A.II.3)
A.II.4
Carrier 2 (B.I.2)
Patient 2 (B.II.1)
Carrier 3 (C.I.1)
C.I.2
Patient 3 (C.II.1)
Patient 4 (C.II.2)
Patient 5 (C.II.3)
Patient 6 (C.II.4)
B
Relative mRNA level
Interferon signature genes
IFI27
IFI44L
IFIT1
ISG15
RSAD2
SIGLEC1
Control
Control IFNα+β (36; 109.7)
AGS patient (28; 10.6)
SAVI (17; 22.7)
A.I.1 (52; 4.1)
A.I.2 (47; 0.9)
A.II.1 (20; 3.8)
A.II.2 (17; 1.2)
A.II.3 (14; 5.1)
A.II.4 (5; 4.3)
B.I.2 (/; 1.1)
B.II.1 (6; 23.2)
C.I.1 (/, 0.2)
C.I.2 (/, 1.3)
C.II.1 (/, 1)
C.II.2 (/, 1.3)
C.II.3 (/, 1)
C.II.4 (/, 5.2)
C
IFN score
CRP (mg/l)
a Mycophenolic acid, Rituximab, Antibiotic prophylaxis
b Sirolimus
c Low-dose Methylprednisolone
d Ruxolitinib
* High-dose Methylprednisolone
** Alveolar lung hemorraghe
D
Control
STAT1 GOF
A.II.3 (p.R1142X)
Count
pY701-STAT1-PE
IFN-γ + staurospoine 60 min
IFN-γ + staurospoine 30 min
IFN-γ + staurospoine 15 min
IFN-γ + pervandate
IFN-γ
Unstimulated (medium)
E
STING
Giantin
Nucleus
Merge
Control
Carrier 1 A.I.1
Patient 1 A.II.3
Patient 2 B.II.1
p.R1142X
p.R1058C
Control
A.I.1
C.I.1
C.II.4
A.II.3
C.II.1
C.II.2
C.II.3
F
Fibroblasts
EBV LCL
Pearson coefficient (Golgi - Sting colocalization)
Control1
Control2
Control3
Control4
Carrier 1 (A.I.1)
Patient 1 (A.II.3)
Patient 2 (B.II.1)
A.I.1
A.II.3
C.I.1
C.II.1
C.II.2
C.II.3
C.II.4

Figure 6

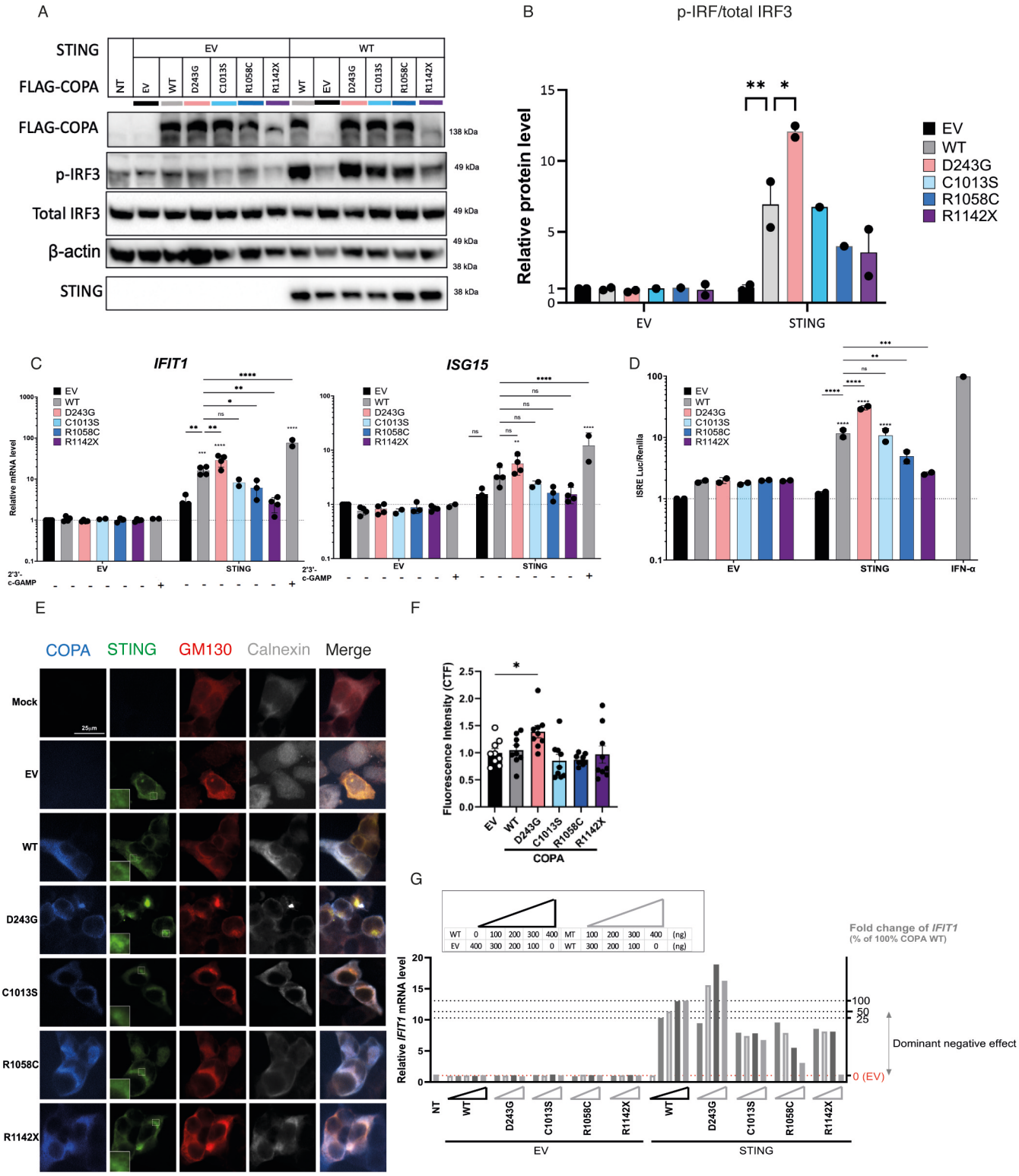
A
STING
FLAG-COPA
NT
EV
WT
D243G
C1013S
R1058C
R1142X
FLAG-COPA
p-IRF3
Total IRF3
β-actin
STING
138 kDa
49 kDa
49 kDa
49 kDa
38 kDa
38 kDa
B
p-IRF/total IRF3
Relative protein level
EV
STING
C
IFIT1
ISG15
Relative mRNA level
2'3'-c-GAMP
D
ISRE Luc/Renilla
IFN-α
E
COPA
STING
GM130
Calnexin
Merge
Mock
25μm
F
Fluorescence Intensity (CTF)
COPA
G
Relative IFIT1 mRNA level
Fold change of IFIT1
(% of 100% COPA WT)
Dominant negative effect
0 (EV)

Figure 7

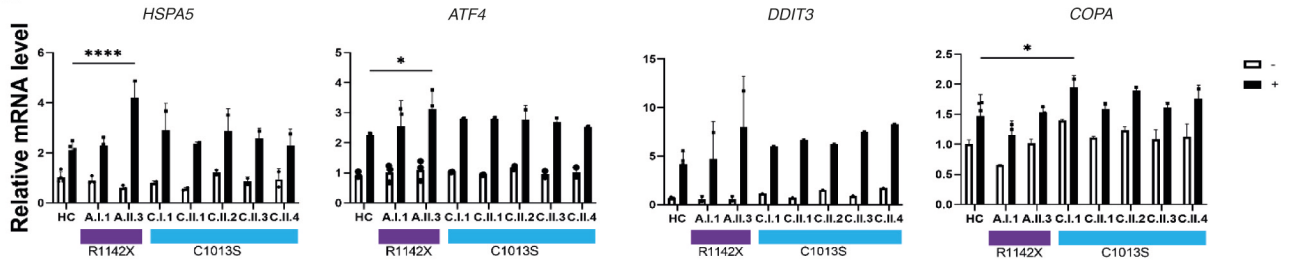
A
HSPA5
ATF4
DDIT3
COPA
Relative mRNA level
HC A.I.1 A.II.3 C.I.1 C.II.1 C.II.2 C.II.3 C.II.4
R1142X
C1013S
-
+

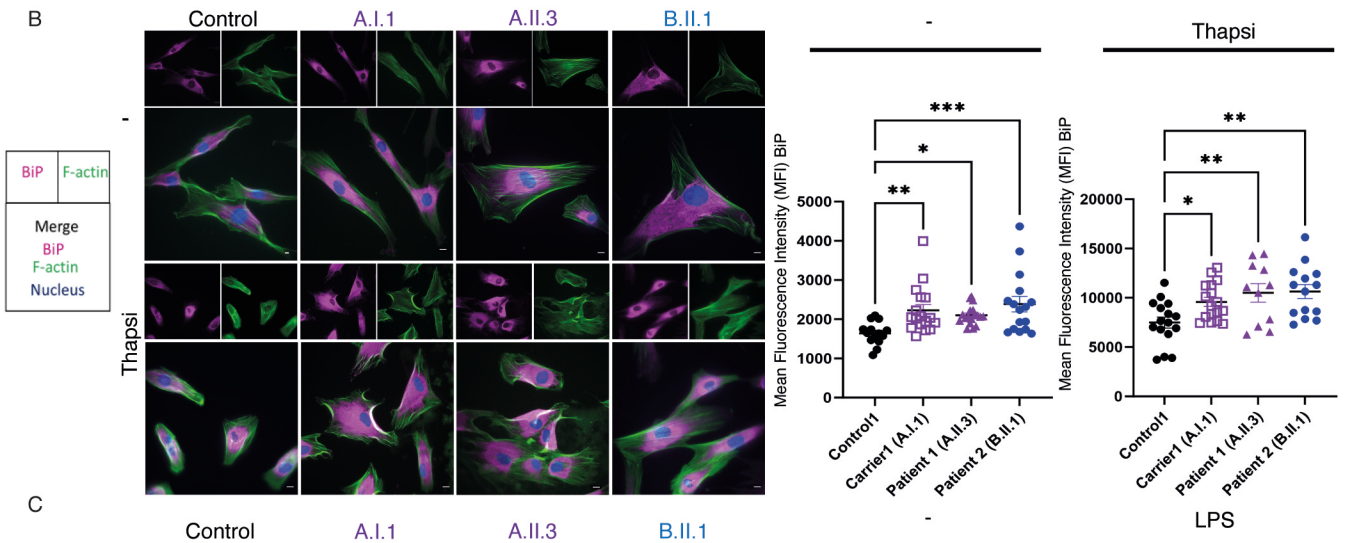
B
Control
A.I.1
A.II.3
B.II.1
BiP
F-actin
Merge
BiP
F-actin
Nucleus
Thapsi
Mean Fluorescence Intensity (MFI) BiP
Control1
Carrier1 (A.I.1)
Patient 1 (A.II.3)
Patient 2 (B.II.1)

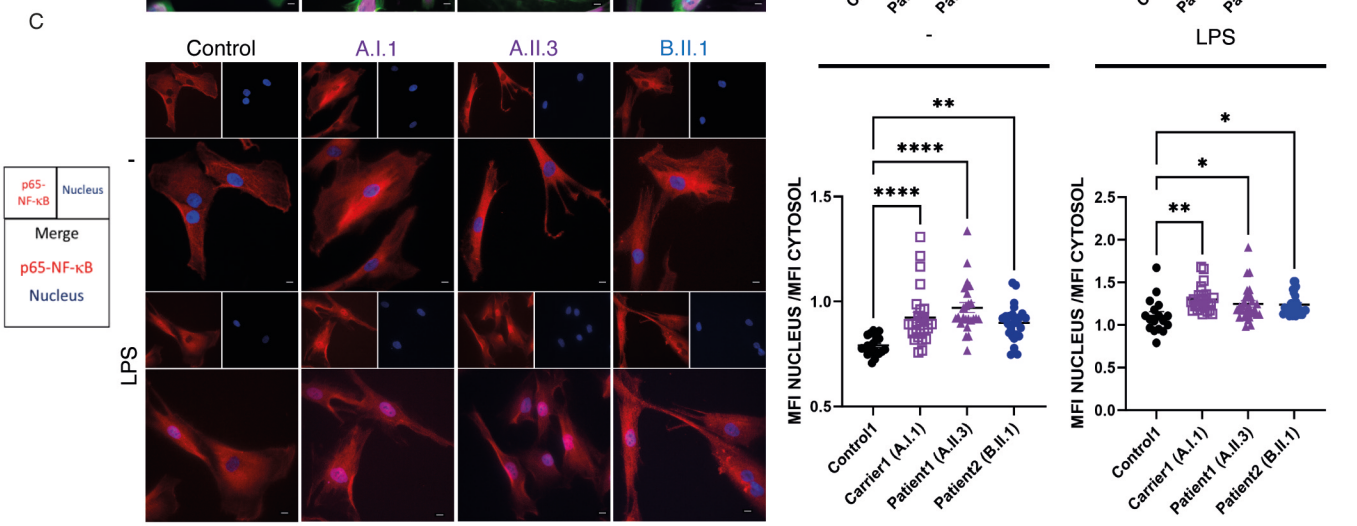
C
Control
A.I.1
A.II.3
B.II.1
p65-NF-κB
Nucleus
Merge
p65-NF-κB
Nucleus
LPS
MFI NUCLEUS /MFI CYTOSOL
Control1
Carrier1 (A.I.1)
Patient1 (A.II.3)
Patient2 (B.II.1)

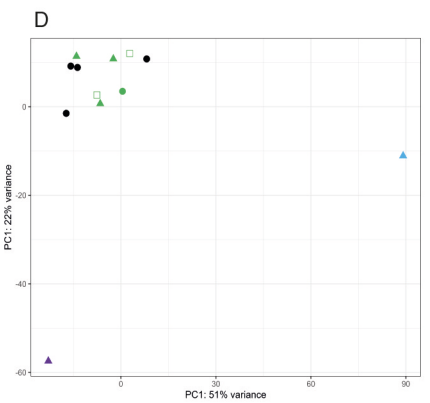
D
PC1: 22% variance
PC1: 51% variance
Group
Control
Carrier
Patient
SAVI
A.II.3
C.II.4

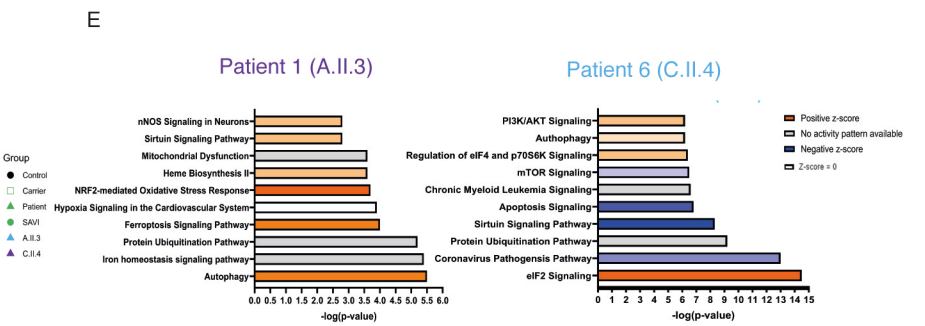
E
Patient 1 (A.II.3)
Patient 6 (C.II.4)
nNOS Signaling in Neurons
Sirtuin Signaling Pathway
Mitochondrial Dysfunction
Heme Biosynthesis II
NRF2-mediated Oxidative Stress Response
Hypoxia Signaling in the Cardiovascular System
Ferroptosis Signaling Pathway
Protein Ubiquitination Pathway
Iron homeostasis signaling pathway
Autophagy
PI3K/AKT Signaling
Authophagy
Regulation of eIF4 and p70S6K Signaling
mTOR Signaling
Chronic Myeloid Leukemia Signaling
Apoptosis Signaling
Sirtuin Signaling Pathway
Protein Ubiquitination Pathway
Coronavirus Pathogensis Pathway
eIF2 Signaling
Positive z-score
No activity pattern available
Negative z-score
Z-score = 0
-log(p-value)

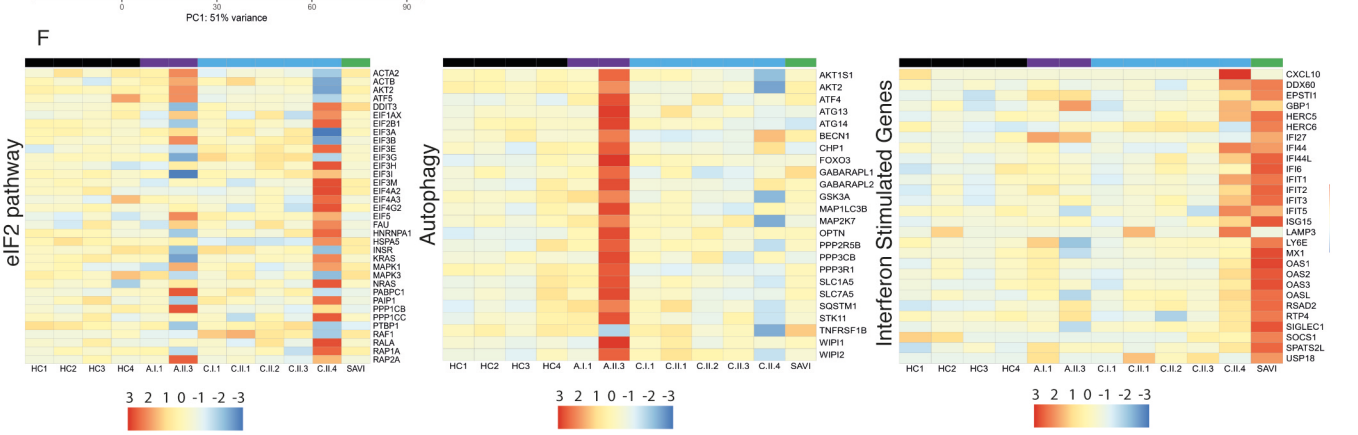
F
eIF2 pathway
Autophagy
Interferon Stimulated Genes
HC1 HC2 HC3 HC4 A.I.1 A.II.3 C.I.1 C.II.1 C.II.2 C.II.3 C.II.4 SAVI
3 2 1 0 -1 -2 -3